

Real-Time Signal Processing and Hardware Development for a Wavelength  
Modulated Optical Fiber Sensor System

by

Shah M. Musa

Dissertation submitted to the Faculty of the  
Virginia Polytechnic Institute and State University  
in partial fulfillment of the requirements for the degree of

Doctor of Philosophy

in

Electrical and Computer Engineering

Approved

Kent A. Murphy, Chair

Richard O. Claus

Jeffrey H. Reed

Roger L. Simpson

Anbo Wang

June 26, 1997

Blacksburg, Virginia

Keywords: Real-time DSP, optical fiber sensor, extrinsic Fabry-Perot interferometer, fiber Bragg  
grating sensor

Copyright 1997, Shah M. Musa

# Real-Time Signal Processing and Hardware Development for a Wavelength Modulated Optical Fiber Sensor System

by

Shah M. Musa

Kent A. Murphy, Chairman

The Bradley Department of Electrical and Computer Engineering, Virginia Tech

## (ABSTRACT)

The use of optical fiber sensors is increasing widely in civil, industrial, and military applications mainly due to their, (a) miniature size, (b) high sensitivity, (c) immunity from electro-magnetic interference, (d) resistance to harsh environments, (e) remote signal processing ability, and, (f) multiplexing capabilities. Because of these advantages a variety of optical fiber sensing techniques have evolved over the years having potentials for myriad of applications. One very challenging job, for any of these optical fiber sensing techniques, is to implement a stand alone system with the design and development of all the signal processing models along with the necessary hardware, firmware, and software satisfying the real-time signal processing requirements. In this work we first develop the equations for the system model of the wavelength modulated extrinsic Fabry-Perot interferometric (EFPI) optical fiber sensor, and then design and build all the hardware and software necessary to implement a stand-alone system, satisfying all the requirements of the real-time signal processing capabilities. We also present the real-time system constructions and the signal processing techniques for the fiber Bragg grating (FBG) and the long period grating (LPG) sensors, and develop all the necessary signal processing software for the FBG system. The Texas Instruments TMS320C40 floating point digital signal processing (DSP) chip is used as the mother processor for the system. All the hardware and software necessary to interface the stand alone system to the Internet is also designed and developed, and one can establish a client/server environment using the TCP/IP protocol suite to acquire data, and/or monitor or control the system, using computers having Internet IP addresses assigned to them.

## Acknowledgments

I would like to thank Dr. Kent Murphy, Dr. Richard Claus, Dr. Anbo Wang, Dr. Jeffrey Reed, and Dr. Roger Simpson for serving on my committee and providing all the thoughtful suggestions. It has been both a pleasure and an honor to work with all of them.

I would like to express my special gratitude and appreciation to Dr. Kent Murphy, for accepting me to work with him as a graduate student, and for providing me with all the resources for this work.

I am grateful to Tracy Cramer, who did the overall design of the 'C40 board, William Cockey, who did all the PCB layout for the boards, John Turman, who did all the populations for the boards, Frank Greenley, who took all the pains to do all the signal tracings and corrections to make the system work, and Paul Duncan, my mentor both in the hardware and the software world, who made all the decisions, supervisions, and corrections all along the entire work. My own contribution in the hardware part, were mainly in designing the analog-to-digital conversion (ADC) board, designing the interfacing connections of the boards, and designing and developing the Xilinx FPGAs for the 'C40 board. I wish to thank Dr. Kevin Shinpaugh, Tracy Cramer, and Steve Poland for providing me many of the real-time signal processing algorithms for this work. I wish to thank all the people of F&S Inc., Blacksburg and of FEORC, Virginia Tech, for providing me such an excellent research environment.

I am thankful to my parents and all my brothers and sisters for providing me support, morally and financially, to come to Virginia Tech for graduate studies. I am greatly thankful to my wife Aliya Shafquat, who herself being a full-time graduate student of Virginia Tech, managed to do all the works of home and at the same time raise our newborn Zuhayeer Hammam Musa, who is only eight months old now. And above all, I am thankful to Allah for providing me with all the opportunities to work with this project and making it possible to complete it.

## Table of Contents

<b>Chapter 1. Introduction</b> .....	1
1.1 Applications of Optical Fiber Sensors.....	1
1.2 Optical Fiber Sensing Techniques.....	4
1.2 Wavelength Modulated Optical Fiber Sensors.....	7
1.3 Objective and Scope.....	8
1.4 Organization of the Dissertation.....	9
<b>Chapter 2. The Wavelength Modulated EFPI Sensor System</b> .....	11
2.1 Construction of the Real-Time Wavelength Modulated EFPI Sensor System.....	11
2.2 The System Signal Response.....	13
2.3 Modeling the Wavelength Modulated EFPI Sensor System.....	13
2.4 Demodulation Techniques of the Signal Response.....	19
2.4.1 Peak-to-Peak Method.....	19
2.4.2 FFT Method.....	23
2.4.3 Discrete Gap Transform Method.....	25
2.4.4 FFT and then Discrete Gap Transform with Golden Search Rule.....	27
<b>Chapter 3. The FBG and The LPG Sensor Systems</b> .....	40
3.1 Construction and Signal Response of the FBG Sensor System.....	40
3.2 Construction and Signal Response of the LPG Sensor System.....	41
3.3 Fabrication of the FBG and the LPG Sensors.....	42
3.4 Principle of Operations of the FBG and the LPG Sensor Systems.....	43
3.5 Demodulation Techniques for the Signal Response of the Real-Time FBG Sensor System.....	46
3.6 Demodulation Techniques for the Signal Response of the Real-Time LPG Sensor System.....	48
3.7 Summary of the FBG and the LPG Sensor Systems.....	48

<b>Chapter 4. Hardware Development.....</b>	<b>54</b>
4.1 S1000 Linear Array CCD Spectrometer.....	54
4.2 Analog-to-Digital Conversion Board.....	55
4.3 TMS320C40 Board.....	56
4.4 Programming the Logic for the Xilinx FPGA XC4003A-4PC84.....	59
<b>Chapter 5. Firmware and Software Development.....</b>	<b>68</b>
5.1 DSP Firmware and Software Development Environment.....	68
5.2 Development of the DSP Firmware and Software.....	69
5.2.1 The Initialization Routines.....	70
5.2.2 The Data Acquisition Routine.....	71
5.2.3 The UART Service Routine.....	72
5.2.4 The EFPI Signal Processing Routines.....	72
5.2.5 The FBG Signal Processing Routines.....	73
5.2.6 The Memory Allocation File.....	74
5.3 The TCP/IP Client/Server Software Development Environment.....	74
5.4 Development of the TCP/IP Client/Server Software.....	74
5.4.1 TCP/IP Client Programs.....	75
5.4.2 TCP/IP Server Programs.....	75
<b>Chapter 6. Performance and Limitations.....</b>	<b>78</b>
6.1 Real-Time Performance of the Wavelength Modulated EFPI Sensor System.....	78
6.2 Real-Time Performance of the FBG Sensor Systems.....	79
6.3 Limitations of the Sensor Systems.....	80
6.4 Noise Issues.....	81
6.5 Comparisons of the Sensor Systems.....	81
<b>Chapter 7. Conclusions.....</b>	<b>83</b>
7.1 Summary and Conclusions.....	83
7.2 Future Enhancements.....	84

<b>Appendix A. The Real Time Signal Processing Firmware and Software.....</b>	<b>87</b>
A.1 Real-Time Signal Processing Routines for the EFPI Sensor System.....	87
A.2 Real-Time Signal Processing Routines for the FBG Sensor System.....	113
A.3 Memory Allocation for the Real-Time Optical Fiber Sensor Systems.....	118
<b>Appendix B. The TCP/IP Client/Server Software.....</b>	<b>119</b>
B.1 The TCP/IP Client Graphical User Interface.....	119
B.2 The TCP/IP Client Software Routines.....	120
B.3 The TCP/IP Server Graphical User Interface.....	126
B.4 The TCP/IP Server Software Routines.....	126
<b>Appendix C. The Matlab Codes for the Simulation and the Signal Processing.....</b>	<b>133</b>
C.1 Matlab Code to Simulate the Signal Response of the Wavelength Modulated EFPI Sensor System.....	133
C.2 Matlab Code for the FFT Method of the Wavelength Modulated EFPI Sensor System, to Find the EFPI Gap Length $g$ .....	134
C.3 Matlab Code for Discrete Gap Transformation on the Data of the Wavelength Modulated EFPI Sensor System, to Find the EFPI Gap Length $g$ .....	135
<b>References.....</b>	<b>136</b>
<b>Vita.....</b>	<b>144</b>

## List of Figures

Figures are loaded at the end of each chapter.

<b>Figure 2.1</b> .....	28
Construction of the real-time wavelength modulated EFPI sensor system.	
<b>Figure 2.2</b> .....	29
Signal response of the wavelength modulated EFPI sensor system with the Ocean Optics S1000 linear array spectrometer of SIE-687, and an EFPI gap of 50.0 micrometer.	
<b>Figure 2.3</b> .....	30
Signal response of the wavelength modulated EFPI sensor system with the Ocean Optics S1000 linear array spectrometer of SIE-687, and an EFPI gap of 80.0 micrometer.	
<b>Figure 2.4</b> .....	31
Electric field distribution across the cross-section of the single-mode fiber.	
<b>Figure 2.5</b> .....	32
Loss effect in coupling the optical power back into the input/output fiber after the reflection at the sensing interface.	
<b>Figure 2.6</b> .....	33
Phasor addition of two waves of amplitude $\alpha$ and $\beta$ having the same frequency and a difference of phase of $\delta$ .	

<b>Figure 2.7</b> .....	34
Simulated signal response of the wavelength modulated EFPI sensor system model for an EFPI gap of 50.0 micrometer and other parameters as given in Appendix C.1.	
<b>Figure 2.8</b> .....	35
The filtered data of a wavelength modulated EFPI sensor system, which uses the Ocean Optics S1000 linear array spectrometer of SIE-687, and has an EFPI air gap of 80 $\mu\text{m}$ . The filter used is of high-pass Butterworth of order 3 and of normalized cutoff frequency of 0.03.	
<b>Figure 2.9</b> .....	36
The FFT implementation on the filtered data of a wavelength modulated EFPI sensor system, which uses the Ocean Optics S1000 linear array spectrometer of SIE-687, and has an EFPI air gap of 80 $\mu\text{m}$ .	
<b>Figure 2.10</b> .....	37
Index of the 1024 active elements, of the Ocean Optics S1000 linear array spectrometer of SIE-687, versus their corresponding wavelengths. Note that the curve is not linear due to non-uniform spacing in wavelengths between adjacent elements.	
<b>Figure 2.11</b> .....	38
Magnitude of discrete gap transformation (DGT) of 11 sets of data, acquired with the wavelength modulated EFPI sensor system with a nominal EFPI gap of 50 $\mu\text{m}$ and increasing the gap by 1 $\mu\text{m}$ at each step. The system uses the Ocean Optics S1000 linear array spectrometer of SIE-687. Note that, there are about couple of $\mu\text{m}$ of offset between the nominal values and the calculated ones.	

<b>Figure 2.12</b> .....	39
Calculated EFPI gap using the FFT method and the DGT method, both using the same 7 sets of data acquired from a wavelength modulated EFPI sensor system with a nominal EFPI gap of 50 $\mu\text{m}$ , using the Ocean Optics S1000 linear array spectrometer of SIE-687. For all the 7 data sets, every parameter of the system is the same, the only difference is the noise. Note the relative precision of the DGT method compared than that of the FFT method.	
<b>Figure 3.1</b> .....	49
Construction of a real-time FBG sensor system. The system shows two sensors multiplexed on the same fiber, but having different reflection frequencies.	
<b>Figure 3.2</b> .....	50
Signal response of an FBG sensor system with two sensors multiplexed on the same fiber. One sensor has a reflection wavelength of 852.6 nm and the other has a reflection wavelength of 862.3 nm	
<b>Figure 3.3</b> .....	51
Construction of a real-time LPG sensor system. The system having two sensors multiplexed on the same fiber, but with different transmission loss frequencies.	
<b>Figure 3.4</b> .....	52
Signal response of an LPG sensor. Note that, there are several dips in the transmission spectrum, each dip corresponds to the coupling of the fundamental guided mode to a different cladding mode. The intensity in dB is shown relative to the highest transmission loss in the spectrum.	

<b>Figure 3.5</b> .....	53
Phase matching conditions of mode coupling for (a) Bragg or short period gratings, and (b) long period gratings [Veng96]. The smaller the differential phase propagation constant $\Delta\beta$ , the longer the period of gratings $\Lambda$ .	
<b>Figure 4.1</b> .....	61
S1000 Linear CCD Array Spectrometer of Ocean Optics, Inc. (The card-edge connects to a set of 12-pin headers on the ADC board using a 44-pin card-edge connector and a ribbon cable.)	
<b>Figure 4.2</b> .....	62
The analog-to-digital conversion (ADC) board. (A 32-pin socket, located on the back-side of the ADC board, directly connects to a set of 32-pin headers, on the back-side of the ‘C40 board.)	
<b>Figure 4.3</b> .....	63
Interface connections of the CCD Spectrometer, the ADC chip, and the TMS320C40 chip.	
<b>Figure 4.4</b> .....	64
The TMS320C40 real-time signal processing board, which holds the ‘C40 processor, the UART, SRAM, non-volatile SRAM, watchdog timekeeper, and the Xilinx FPGAs.	
<b>Figure 4.5</b> .....	65
Top level schematic of the programmed logic for the Xilinx FPGA XC4003A-4PC84 to generate, buffer, and interface the control signals of the C40 local buses, the PC16550D UART, and the SRAM memory devices.	

**Figure 4.6**.....67

Top level schematic of the programmed logic for the Xilinx FPGA XC4003A-4PC84 to generate, buffer, and interface the control signals of the C40 global buses, and the non-volatile SRAM memory devices.

**Figure 5.1**.....77

Block level diagram of the networking connections of the real-time wavelength modulated sensor system with the Internet.

# Chapter 1

## Introduction

Even after nearly 30 years since its first introduction, new ideas in applications and sensing techniques is still evolving for optical fiber sensors [Culs95]. The use of optical fiber sensors is increasing widely in civil, industrial, and military applications mainly due to their, (a) miniature size and light weight, (b) high sensitivity, (c) immunity from electro-magnetic interference, (d) resistance to harsh environments, (e) remote signal processing abilities, and, (f) multiplexing capabilities [Udd91]. We discuss below the major applications and techniques of optical fiber sensors. The wavelength modulated optical fiber sensor systems and their advantages, and the overall objective and organization of this dissertation are also presented.

### 1.1 Applications of Optical Fiber Sensors

The areas of applications of optical fiber sensors have evolved to be very wide and vast over the years. Fiber optic sensors are attractive as they have excellent sensitivity, wide dynamic range, compact and rugged construction, and high reliability. Some of the major applications which have been implemented, demonstrated, or proposed for optical fiber sensors are discussed below.

#### *Measurement of strain:*

Optical fiber sensors have been shown to measure strain in a multitude of ways [Flav95, Sirk95, Zimm89]. Strain measurement has also been implemented with distributed and multiplexed sensors [Hori95]. Due to light weight, minute size, and remote interrogation capabilities of

optical fiber sensors strain measurements of structures with imbedded sensors have also been implemented [Habe95, Lesk92].

*Measurement of temperature:*

Optical fiber sensors for the measurement of temperature have been widely demonstrated, implemented, and commercialized[Dils83], with a wide variety of applications including the measurement of temperature in nuclear reactors [Gott81, Meun95]. Measurement of temperature in high electro-magnetic field or in high radiation is possible with optical fiber sensors [Fern95]. Temperature can also be measured with distributed or multiplexed fiber sensors [Bao95].

*Measurement of pressure:*

Fiber optic sensors can be used for measurements of pressure[Wang92]. Measurement of pressure in boilers, chemical process reactors, combustion engines, airplane wings, and human body can be implemented with optical fiber sensors [Udd91].

*Measurement of current, magnetic field, and voltage:*

Optical fiber sensors have been reported to measure current, magnetic field, and voltage [Culs88, Fang96, Buch95]. Measurement of current at high voltage has been implemented [Roge73]. Vectorial measurement of magnetic field has been demonstrated using optical fiber sensors [Anno92]. Voltage measurement using liquid-core optical fiber sensor has also been demonstrated [Kuri83].

*Acoustic sensor:*

Optical fiber sensors have been demonstrated to detect weak acoustic signals [Buca77, Cole77]. It has been used as a “point”, “gradient”, or “directional” sensing device for the purpose of designing hydrophone [Culs88]. It has also been used to detect signals of surface acoustics [Tran91].

*Vibration sensor:*

One of the uses of optical fiber sensor is the vibration measurements [Murp92b, Yu95]. Vibration in the range of 1.4 Hz to 85 kHz has been demonstrated to be accurately measured by an optical fiber sensor [Lima96]. Optical fiber sensors have been proposed to measure the high temperature seismic events of the deep boreholes and the volcanic regions of the earth surface [Jack96].

*Displacement sensor:*

Optical fiber sensors has been demonstrated and used as high precision displacement sensors, specially, for applications where micrometer or nanometer resolutions are required over short dynamic ranges [Rama88, Wade85, Wang95]. Optical fiber sensors has been proposed for the accurate measurement of the relative drift of the floors of the multistoried buildings when they undergo wind or earthquake loading [Benn96].

*Chemical sensor:*

Due to its inert and nonelectrical nature and remote sensing abilities optical fiber sensors are commercially being used for sensing various chemical materials. Fiber optic sensors can be used for detection or measurement of the concentration of various toxic or explosive gases such as CO, CH<sub>4</sub>, C<sub>2</sub>H<sub>6</sub>, N<sub>2</sub>O, and SO<sub>2</sub> [Jeff85, Inab79, Hord83, Chan84]. Optical fiber sensors have also been demonstrated to be used for in-situ composite cure monitoring [Luo96, Druy88]. Fiber optic sensors can be used for food processing, photographic and similar chemical processing, hazardous waste analysis, groundwater monitoring, and stack gas analysis [Mila83, Udd91].

*Biomedical sensor:*

One of the most significant applications of optical fiber sensors is in biomedical engineering [Pete84, Mign95]. Optical fiber sensors have been demonstrated to measure or detect pH (hydrogen ion concentration) for both clinical or non-clinical purposes [Mark81, Pete80, Mich95, Debo95]. A fiber optic sensor has been demonstrated to accurately measure the concentration of glucose [Mans84]. Optical fiber sensors can be used to measure the velocity of blood flow of

vessels [Tana75], or the temperature or pressure of any part of the human body, by guiding the sensor fiber within a catheter tube [Culs88].

*Embedded sensor for smart materials and smart structures:*

Optical fiber sensors are considered to be one of the prime candidates for smart materials and smart structures [Meas92, Urru88, Wood89]. Due to its light weight, miniature size, multiplexing capabilities, and remote interrogation abilities fiber optic sensors have aptly been imbedded in building beams or bridge columns for nondestructive evaluation of these structures [Nell96].

## **1.2 Optical Fiber Sensing Techniques**

In an optical fiber sensor system the change of the measurand changes one or more optical properties of the sensor creating a change in electrical measurables like voltage or current by optical-to-electrical conversion using photodetectors, and thus enable any measurements to be performed through the information of optics. As the optical wavelengths are measured in the units of nanometers and the responsivity of photodetectors are very high, very precise measurement of the measurand is possible through fiber optic sensors.

Techniques of implementations of optical fiber sensors are very wide and broad. Some of the major sensing techniques of optical fiber sensors are discussed here. Note that many of these techniques have a displacement resolution reported in the order of nanometers or even in picometers [Grat95, Murp92].

*Intensity based sensor:*

The basic concept of intensity based sensors is very simple, either the reflective or the transmissive intensity of light is modulated by the measurand [Laga81, Cork88, Laws83, Bert87]. The major limitation of any intensity based sensor is the lack of any suitable reference intensity signal. Any intensity fluctuations in the output not associated with the measurand produce erroneous results [Udd91].

*Fabry-Perot interferometric sensor:*

In Fabry-Perot interferometric sensor there are two reflective surfaces enclosing a Fabry-Perot (FP) cavity of an optically transparent medium [Born75]. The reference signal and the sensing signal reflects from these two interfaces, and the interfered signal is monitored. Any change of measurand changes the length and/or any other optical properties of the FP cavity, causing a change in the interfered signal. Depending on the type of the cavity, the sensor can be termed either as intrinsic FP interferometric (IFPI) sensor, or extrinsic FP interferometric (EFPI) sensor. For the case of EFPI sensor the FP cavity is formed outside the optical fiber [Clau92].

*Mach-Zehnder interferometric sensor:*

In a Mach-Zehnder interferometric sensor the coherent light source is launched into a single-mode fiber, which is then split into two arms, using a fiber optic coupler, the sensing arm and the reference arm [Udd91]. These two arms are then recombined using a second fiber optic coupler known as recombiner. The recombined, or the interfered, signal is detected by a photodetector. Any change of measurand changes the phase of the coherent signal of the sensing arm, causing an appropriate change in the detected signal.

*Michelson interferometric sensor:*

The main difference of a Michelson interferometric sensor compared to a Mach-Zehnder one is that light is reflected back by mirror from both the reference arm and the sensing arm and then recombined by the same coupler which split them [Mali96]. So there is only one 2X2 coupler for a Michelson interferometer, in one side of the coupler is the sensing arm and the reference arm

(both having mirrors at the ends), and on the other side of the coupler is the optical source and the detector. The detector detects the interfered (or recombined) signal which changes with the change of measurand on the sensing arm.

*Sagnac Interferometric sensor:*

In Sagnac interferometric sensor beams of light propagate in clockwise and counterclockwise directions inside an optical fiber ring. When the ring of fiber rotates in the clockwise direction, the optical beam propagating in the clockwise direction traverses a light path longer than the light path traversed by the counterclockwise beam (which is known as Sagnac effect). Any change of speed of rotation of the fiber ring changes the difference of the optical paths between these two counter-propagating beams [Udd91].

*White light interferometric sensor:*

When the system light source, in interferometric sensor systems discussed above, is of wide band, rather than of a single coherent frequency, it is termed a white light interferometric sensor system. In white light interferometric systems the sensor is interrogated over a wide band of optical frequencies (or wavelengths) and the signal response is acquired and processed for the entire band. The white light interferometric systems have several inherent advantages, though their signal processing techniques are more complex than that of single frequency systems. Among the advantages are the precise and accurate measurements, the self calibrating capabilities, and the wide unambiguous dynamic range of operations [Chen92].

*Absorption spectroscopic sensor:*

In absorption spectroscopic sensors the measurand causes some of the spectrum of the wide band light source transmitted through an optical fiber to be absorbed or attenuated [Grat95]. These types of techniques are widely used in chemical sensors.

*Fiber Bragg grating (FBG) sensor:*

Bragg gratings are periodic refractive index variations written into the core of an optical fiber by exposure to an intense UV interference pattern [Melt96]. For an FBG sensor, changes of measurand are encoded as changes in the periodicity or refractive index of the grating and thereby shifting the wavelength of the reflected wave [Jone95]. The measurements of the measurand is achieved by detecting the wavelength of the reflected wave.

*Long period grating (LPG) sensor:*

One of the newest techniques in the optical fiber sensor technology is the LPG sensor [Veng96]. While in an FBG sensor, coupling of energy occurs from the forward propagating fundamental mode to the reverse propagating fundamental mode, coupling of energy in an LPG sensor occurs from the forward propagating fundamental mode to the forward propagating cladding modes, which attenuate very rapidly due to the lossy cladding-coating interface. The measurements of the measurand is thus achieved by detecting the attenuated wavelength in the transmission spectrum.

### **1.3 Wavelength Modulated Optical Fiber Sensors**

In a wavelength modulated optical fiber sensor usually a wide band source is employed. A change in measurand of such a system causes wavelength dependent intensity variations over the spectrum of the source. By using diffraction gratings and charged coupled device (CCD) elements, a graph of wavelength versus intensity of the optical output can be achieved for the whole spectrum of the source. The measurements of the measurand can be achieved by processing the measurand-induced wavelength dependent intensity modulated signals, i.e. by processing the wavelength versus output intensity graph.

Note that, any system using white light interferometric sensors, absorption spectroscopic sensors, FBG sensors, or LPG sensors can be generalized as a system of wavelength modulated optical fiber sensor.

There are some distinct advantages of wavelength modulated optical fiber sensor systems over other types of sensor systems like intensity modulated systems or single frequency interferometric sensor systems. Among the advantages are:

- Accuracy of measurements are independent of small intensity variations of the source of the system.
- The unambiguous range of the movement of the sensing fiber is not limited to only quarter of a wavelength of a single frequency source, rather a wide dynamic range is achieved [Chen92].
- The sensitivity of the sensor is independent of the variations of the measurand.
- Since the information about the measurand is inscribed over a wide band rather than over a single frequency, a higher measuring precision and accuracy is achieved.
- A single low cost wide band source like LED is required rather than expensive quadrature phase-shifted coherent laser sources [Murp91].
- Direct measurement of strain and self calibrating qualities are achieved for Fabry-Perot interferometric types of sensors.

## **1.4 Objective and Scope**

Because of the advantages of a wavelength modulated optical fiber sensor system, as stated earlier, a great amount of recent work in fiber sensor technology has been focused on the utilization of the white light interferometric sensing techniques[Mars96, Chen92], or on other types of wavelength modulated techniques such as FBG or LPG sensing techniques [Davi95]. In this work we develop a complete model of a wide-band extrinsic Fabry-Perot interferometric

(EFPI) sensor system, along with the development of all the associated equations. The model provides an insight to the modulation of the signal response and their demodulation techniques. We then design and build all the hardware and software necessary to implement a stand-alone system, which is capable of digitizing and processing the EFPI sensor signals over the whole spectrum of the wide source, and producing the precise and accurate measurements, all in real-time. We present the real-time system constructions and their signal processing techniques for the fiber Bragg grating (FBG) and the long period grating (LPG) sensors, and develop all the necessary signal processing software for the FBG system. The Texas Instruments TMS320C40 floating point digital signal processing (DSP) chip is used as the mother processor for the system.

We also design, develop and implement the interfaces and the associated client/server software necessary to interconnect the wavelength modulated optical fiber sensor system to the Internet. One can easily establish a client/server environment using the TCP/IP protocol suite to acquire data, and/or monitor or control the system, using computers having Internet IP addresses assigned to them.

## **1.5 Organization of the Dissertation**

This dissertation is organized in seven chapters. Chapter 2 deals with the EFPI sensor systems. It develops the theory for modeling the EFPI system, and presents different signal processing techniques for the system. The FBG and the LPG sensor systems are dealt in Chapter 3. Chapter 4 describes the issues concerned with the development of the hardware, and Chapter 5 describes the issues concerned with the firmware and the software. Chapter 6 presents the performance and limitations of our system. Chapter 7 provides the conclusions and suggestions for future enhancements.

In the appendix, we provide some of the firmware and software we developed for acquiring data and processing signals for the system. Also included are the client/server graphical user interface (GUI) software developed in National Instruments LabWindows CVI for the Internet connectivity of the system, and the Matlab simulation codes for the system models and data analysis.

## Chapter 2

### The Wavelength Modulated EFPI Sensor System

In this chapter we present the construction, the signal response, and the signal processing techniques of the wavelength modulated extrinsic Fabry-Perot interferometric (EFPI) sensor system. Equations are derived to model the behavior of the wavelength modulated EFPI sensor system, which provide an insight to the modulation of the signal responses and their demodulation techniques. Several demodulation techniques are presented along with their merits and demerits.

#### 2.1 Construction of a Real-Time Wavelength Modulated EFPI Sensor System

Figure 1 shows the basic functional block diagram of a wavelength modulated EFPI optical fiber sensor system. A broadband super luminescent light-emitting diode (SLED) is employed as an optical source to launch light into a single-mode optical fiber. The broadband light propagates to an EFPI sensor through an optical coupler, and reflects back, first, from the glass-air interface of the input/output fiber, and second, from the air-glass interface of the reflector fiber. The first reflection is termed as the *reference reflection* while the second reflection is termed as the *sensing reflection* [Murp91]. A reflection of desired percentage can be achieved from the 2nd interface by applying appropriate coating material to the reflector fiber. The other end of the reflector fiber is shattered roughly to scatter away any light that transmits through it, and thus there is no reflection from that end. Interference occurs in the input/output fiber between the backward propagating waves of the reference reflection and the sensing reflection, and depending on the length of the EFPI air gap some wavelengths add with a phase difference of  $360^\circ$  (or a

multiple of  $360^\circ$ ) producing fringe peaks, and some wavelengths add with a phase difference of  $180^\circ$  (or an odd multiple of  $180^\circ$ ) producing fringe troughs, and the rest add with a phase difference other than  $360^\circ$  or  $180^\circ$  producing values within the peaks and troughs.

The interfered light propagates back to the end of a fiber through the optical coupler and hits on a reflection diffraction grating, which separates the light components by diffracting different wavelengths at different angles on to a CCD (charge coupled device) array, as shown in Figure 2.1. The CCD array senses the intensity of different wavelength components of the light at different elements of the array and makes an electrical signal pattern with discrete amplitude pulses which corresponds to the linear fringe pattern of the interfered waves, the shape of the pattern depends mainly on the length of the EFPI air gap, the profile of the light launched from the SLED, the responsivity profile of the CCD photo-diodes, and the optical characteristics of the fiber and the coupler. The discrete analog pulses are digitized and transferred to the digital signal processing (DSP) unit, which does all the necessary processing of the digital signal in real-time to find out the length of the air gap of the EFPI sensor.

The sensor system shown in Figure 2.1 is also called an Absolute EFPI (AEFPI) system as it can measure the length of the EFPI air gap and hence the movement (both in direction and in displacement) of the reflector fiber, with respect to the input/output fiber. This capability is unlike the single frequency phase measurement interferometry (PMI), where the direction and the total displacement of the reflector fiber becomes ambiguous over a displacement in excess of  $\lambda/4$  ( $\lambda$  being the wavelength of the light in free space) and also where the absolute position of the reflector with respect to the reference is never known.

## 2.2 The System Signal Response

Figure 2.2 and 2.3 shows the signal responses of the wavelength modulated EFPI sensor system, for an EFPI air gap of 50.0 micrometer and 80.0 micrometer respectively. Due to the Gaussian profile of the SLED optical source, the shape of the signal responses also look like Gaussian, but having the fringe peaks and troughs added with the Gaussian. The signal response with the 80.0 micrometer gap has more number of fringe peaks within the same wavelength range than that of the signal response with the 50.0 micrometer gap. As the length of the EFPI air gap increases, the number of wavelengths which can satisfy the condition of in-phase addition, after being reflected from the reference interface and the sensing interface, also increases, increasing the number of fringe peaks, and decreasing the distance (in terms of wavelength) between adjacent fringe peaks. Note that, the frequency of occurrence of fringe peaks decreases gradually towards the higher end of wavelength values, i.e., there is a chirp present in the frequency of the fringe pattern, for both the Figure 2.2 and 2.3. This chirp is due to the fact that the condition of in-phase addition, after being reflected from the reference interface and the sensing interface, is met more frequently (in terms of wavelength distances) at lower wavelengths, and gradually decreases with the increase of wavelength. In section 2.4.1 we derive mathematical expressions for finding the amount of chirp present in the fringe pattern of any wavelength modulated EFPI sensor system.

## 2.3 Modeling the Wavelength Modulated EFPI Sensor System

Before developing the model equations for the wavelength modulated EFPI sensor system we need to make the assumptions as stated below.

***The model assumptions:***

*Negligible attenuation along the fiber:*

As the commercial single-mode silica fibers have an attenuation about in the range of 0.1 to 0.4 dB/km, and the length of the fiber being used for the system in Figure 2.1 is very short, usually measured only in meters rather than in kilometers, we neglect any attenuation of signal along the fiber.

*Negligible variation in refractive index and insignificant total dispersion:*

SLED is a wide band source and hence the optical wave spectrum launched into the single-mode fiber is also wide. If light of wavelength  $\lambda$ , where  $\lambda$  varies over a range, is launched into the single-mode fiber the index of refraction of the fiber will be different for different values of  $\lambda$ , and for wavelengths less than 1.0  $\mu\text{m}$  the refractive index  $n$  corresponding to any wavelength  $\lambda$  can be found by using the Sellmeier relation [DiDo72],

$$n^2 = 1 + \frac{E_0 E_d}{E_0^2 - E^2}, \quad (2.1)$$

where  $E = hc/\lambda$  is the photon energy corresponding to wavelength  $\lambda$ , and  $E_0$  and  $E_d$  are material oscillator energy and dispersion energy parameters, respectively. For  $\text{SiO}_2$  glass  $E_0 = 13.4$  eV and  $E_d = 14.7$  eV, and also  $hc = 1.24 \mu\text{m}\cdot\text{eV}$  [DiDo72]. For  $\lambda$  ranging from 0.8 to 0.9  $\mu\text{m}$ , the refractive index of the fiber core varies from 1.4532 to 1.4521. The total material dispersion due to this variation of refractive index, though very significant for long-haul fibers having lengths in kilometers, is insignificant for our short length fiber and is neglected. As material dispersion is very dominant over waveguide dispersion at wavelengths lower than 1.0  $\mu\text{m}$  [Keis91], the waveguide dispersion is neglected also.

*Linear polarization with electric vector vibrating parallel to the plane of incidence:*

Optical output from semiconductor light sources are, in general, linearly polarized [Keis91]. We assume that all the waves propagating through the single-mode fiber, either backward or forward, are linearly polarized, i. e., the effect of birefringence is negligible. Birefringence occurs due to circular asymmetry of the fiber rendering unequal velocities to the degenerate modes [Gree93]. We also assume that the electric vector of the mode of our single-mode fiber vibrates parallel (p) to plane of incidence at both the reference and the sensing reflection interfaces, and hence Fresnel's reflection and refraction equations for the  $p$  polarization is used. Figure 2.4 shows the state of electric field at any cross-section of our single-mode fiber.

*Source power launched into the fiber is independent of the power reflected back to source:*

We assume that there is negligible effect on the source due to incidence of optical power propagating back to the source after the reflections. An optical isolator can also be used to hinder the optical power that may propagate back to the source.

*Only the first order reflection in the EFPI cavity is significant:*

There can be multiple reflections inside the EFPI cavity, but the second and the higher order reflections have been shown to have negligible amplitude if compared to the first order reflection [Bhat93], and hence are neglected. We assume only a simple two beam interference system.

*The optical coupler characteristics are independent of wavelength:*

For the wavelength range of our interest we assume that the behavior of the optical coupler, shown in Figure 2.1, is independent of wavelength.

***Development of the model equations:***

If  $g$  is the length of the EFPI air gap, and  $\lambda$  is the free space wavelength of any particular light component, then the field amplitude  $y(\lambda)$  of the interfered light corresponding to wavelength  $\lambda$ , propagating from the EFPI sensor to the reflection grating, under the above assumptions and as shown in Figure 2.1, can be expressed as,

$$y(l) = r_{pr} f_s(l) \cos\left(2p \frac{c}{n_1 l} t\right) + t_{pr} f_a(g) f_s(l) \cos\left(2p \frac{c}{n_1 l} t - \frac{4pg}{l} - j_2 + j_1\right), \quad (2.2)$$

where, i)  $f_s(\lambda)$  is the profile (in terms of amplitude, not intensity) of the SLED light output coupled into the input/output fiber, ii)  $f_a(g)$  is a attenuation factor which can be thought as the square root of the ratio of the light intensity being transmitted out through the first interface to the light intensity being coupled back again into the fiber through the same interface; iii)  $n_1$  is the refractive index of the fiber core (note that  $n_1$  varies negligibly with  $\lambda$ ), iv)  $\phi_1$  and  $\phi_2$  are the reflection phase shifts at the reference and the sensing interfaces respectively (for the first interface of glass-air and for the second interface of air-glass, we get  $\phi_1=0^\circ$  for and  $\phi_2=180^\circ$  [Moll88]), and, v)  $r_{pr}$  and  $t_{pr}$  are Fresnel's amplitude reflection and amplitude transmission coefficients, respectively, for  $p$  polarization, at the reference interface. For normal incidence  $r_{pr} = (n_1-1)/(n_1+1)$ , and  $t_{pr} = 2n_1/(n_1+1)$  [Moll88].  $(4\pi g/\lambda)$  is the phase delay, for any wave of wavelength  $\lambda$ , incurred in traversing the gap length  $g$  forward and backward. Note that Equation (2.2) assumes that, for any  $\lambda$ , the wave reflecting back from the first interface and the wave coupling back again into the fiber through the same interface, are linearly polarized and they have their electric field vectors polarized in the same plane and same direction.

The first term in Equation (2.2) is the reference term while the second term is the sensing term, and both the terms add together to make constructive and destructive fringes for continuous values of  $\lambda$ . The  $f_a(g)$  factor can be approximated with the help of Figure 2.5 and reference [Keis91] as,

$$f_a(g) = r_{ps} \left( \frac{a}{a + g \tan[\sin^{-1}(NA)]} \right)^2 \quad (2.3)$$

where  $r_{ps}$  is Fresnel's amplitude reflection coefficient at the sensing interface,  $a$  is the core radius of the input/output fiber,  $g$  is the gap length between the reference and the sensing reflection interfaces, and NA is the numerical aperture of the input/output fiber.  $NA = (n_1^2 - n_2^2)^{1/2}$ , where

$n_1$  and  $n_2$  are the core and the cladding refractive indices respectively. Note that  $f_a(g)$  is an attenuation factor of amplitude (not intensity) and is independent of  $\lambda$  under the assumption (b).

We can now write Equation (2.2) as,

$$y(l) = f_s(l) \left[ r_{pr} \cos\left(2p \frac{c}{n_1 l} t\right) + t_{pr} f_a(g) \cos\left(2p \frac{c}{n_1 l} t - d\right) \right], \quad (2.4)$$

where  $d = \left(\frac{4pg}{l} + j_2 - j_1\right)$ . Note that Equation (2.4) has two phasor terms of amplitude  $r_{pr}$  and

$t_{pr} f_a(g)$  having the same frequency  $2p \frac{c}{n_1 l}$  with a phase difference of  $\delta$ . The two terms of

Equation (2.4) can be added together with the help of phasor geometry as shown in Figure 2.6, and the resultant vector  $y(\lambda)$  can be written as,

$$y(l) = f_s(l) \underbrace{\left\{ r_{pr} \cos q + t_{pr} f_a(g) \cos(d - q) \right\}}_{\text{amplitude\_factor}} \underbrace{\cos\left(2p \frac{c}{n_1 l} t - q\right)}_{\text{phase\_factor}}, \quad (2.5)$$

where  $q$  is calculated as,

$$q = \sin^{-1} \left[ \frac{t_{pr}^2 f_a^2(g) \sin^2 d}{\left\{ r_{pr} + t_{pr} f_a(g) \cos d \right\}^2 + t_{pr}^2 f_a^2(g) \sin^2 d} \right]^{1/2}. \quad (2.6)$$

As light intensity is proportional to the square of the amplitude of the field, by squaring both sides of Equation (2.5) we can write,

$$\begin{aligned} y^2(l) &= f_s^2(l) \left\{ r_{pr} \cos q + t_{pr} f_a(g) \cos(d - q) \right\}^2 \cos^2\left(2p \frac{c}{n_1 l} t - q\right) \\ &= \frac{1}{2} f_s^2(l) \left\{ r_{pr} \cos q + t_{pr} f_a(g) \cos(d - q) \right\}^2 \left\{ 1 + \cos\left(4p \frac{c}{n_1 l} t - 2q\right) \right\}. \end{aligned} \quad (2.7)$$

The signal current of the photodiode is proportional to the light intensity incident upon the photodetector. Usual photodiodes are not able to respond to double the frequency of light as

expressed by the time varying cosinusoidal term of Equation (2.7), and hence the photo-current,  $I_p$ , sensed by a photodiode can be written as,

$$I_p(l) = A\mathfrak{R}(l)f_s^2(l)\left\{r_{pr}\cos q + t_{pr}f_a(g)\cos(d-q)\right\}^2 \quad (2.8)$$

where  $A$  is a proportionality constant and  $\mathfrak{R}(\lambda)$  is the responsivity of the photodiode. Responsivity  $\mathfrak{R}(\lambda)$  is independent of the power level incident on the photodetector, and is a function of wavelength  $\lambda$  (or in other way is a function of photon energy  $h\nu$ ), and is defined in [Keis91]. For the charged coupled device (CCD) the charge of the photocurrent is stored across a capacitor and accumulated for a period of time to generate a voltage. Using Equation (2.8) the voltage,  $V_c$ , across the CCD capacitor can be written as,

$$V_c(l) = B\mathfrak{R}(l)f_s^2(l)\left\{r_{pr}\cos q + t_{pr}f_a(g)\cos(d-q)\right\}^2, \quad (2.9)$$

where  $B$  is a constant and can be calculated as,  $B = AT/C$ , where  $T$  is the integration period and  $C$  is the capacitance of the CCD elements. Note that the  $f_s^2(l)$  factor of Equation (2.9) can be thought as the optical source profile in terms of intensity, as the  $f_s(\lambda)$  factor in equation (2.1) was considered as the source profile in terms of amplitude.

For practical systems there will be a Gaussian random noise added with the signal of Equation (2.9). Assuming that the noise added is independent of  $l$  and  $g$ , We can write,

$$V_c(l) = B\mathfrak{R}(l)f_s^2(l)\left\{r_{pr}\cos q + t_{pr}f_a(g)\cos(d-q)\right\}^2 + G(m_s^2), \quad (2.10)$$

where  $m$  is the mean and  $s^2$  is the variance of the Gaussian random process.

Equation (2.10) completely models the signal of the wavelength modulated EFPI sensor system of Figure 2.1. For a set of discrete values of  $l$  a set of signals  $V_c(l)$  from Equation (2.10) is achieved. The number of signals in the set is the number of elements of the CCD array, each CCD array element corresponding to a particular  $l$ .

Figure 2.7 shows the simulated signal response of the wavelength modulated EFPI sensor system, modeled by Equation (2.10), for an EFPI gap of 50.0 micrometer and other parameters as given in Appendix C.1.

## 2.4 Demodulation Techniques of the Signal Response

The challenge now is to find out the value of the EFPI air gap length  $g$ , from the complex signal response of the wavelength modulated EFPI sensor system. We have seen that due to the Gaussian profile of the SLED optical source, the shape of the signal response is like Gaussian, but modulated with the fringe pattern, including peaks and troughs. With the increase of the EFPI gap, the number of fringe peaks within the same wavelength range, of the signal response, gets increased, decreasing the distance (in terms of wavelength) between adjacent fringe peaks. Also, the wavelength modulated EFPI sensor system has a signal response where the frequency of occurrence of fringe peaks decreases gradually towards the higher end of the wavelength values, i.e., there is a chirp in the frequency of the fringe pattern, distancing any two adjacent fringe peaks further for larger values of wavelengths.

We present below several methods in reference to process this complicated signal response of the wavelength modulated EFPI sensor system, to find the EFPI gap length  $g$ , and such any measurable that relates to that.

### 2.4.1 Peak-to-Peak Method

Any free space wavelength of value  $\lambda_1$  can make a fringe peak, i.e., can add in-phase after being reflected from the reference interface and the sensing interface, only if it satisfies the condition,

$$2p \frac{2g}{l_1} + j_2 = 2m_1 p + j_1, \quad (2.11)$$

where,  $g$  is the EFPI gap length,  $\phi_1$  and  $\phi_2$  are the reflection phase shifts at the reference and the sensing interfaces respectively, and  $m_1$  is an integer ( $m_1$  represents the number of full wavelengths the wave  $\lambda_1$  travels before adding back in phase). A free space wavelength of value  $l_2$  ( $l_2 > l_1$ ) to make the fringe peak just adjacent to the fringe peak of  $l_1$ , must satisfy the condition,

$$2p \frac{2g}{l_2} + j_2 = 2(m_1 - 1)p + j_1, \quad (2.12)$$

where it is assumed that the reflection phase shifts are independent of wavelengths. Now subtracting Equation (2.12) from Equation (2.11) we get,

$$g = \frac{l_1 l_2}{2(l_2 - l_1)}. \quad (2.13)$$

Thus one can easily find out the EFPI gap length  $g$ , just by finding the wavelengths of the adjacent fringe peaks. The Equation of (2.13) also applies for adjacent fringe troughs, and that can easily be shown using the similar derivation.

As we have observed earlier, the fringe peaks are not uniformly-spaced in wavelengths, rather the wavelength spacing between adjacent fringe peaks increases gradually towards the higher end of wavelength values causing a chirp in the frequency of the fringe pattern. The same is also true for the fringe troughs. Using Equation (2.11) and (2.12) we can easily get,

$$l_2 - l_1 = \frac{8p^2 g}{\{2(m_1 - 1)p + j_1 - j_2\} \{2m_1 p + j_1 - j_2\}}. \quad (2.14)$$

For simplicity let's assume that the reflection phase shifts,  $j_1 = j_2 = 0$ , then we can write the Equation (2.14) as,

$$l_2 - l_1 = \frac{2g}{m_1(m_1 - 1)}. \quad (2.15)$$

Equation (2.15) is of significant importance for the understanding of the chirp phenomena of a wavelength modulated EFPI sensor system. It says that the spacing in wavelength between two adjacent fringe peaks is proportional to the EFPI gap  $g$ , and is inversely proportional to the product of the numbers of full wavelengths the waves, forming the fringe peaks, travels before adding in phase. When  $g$  is constant, as  $m$  decreases for the fringes of the higher wavelengths, the spacing between the adjacent fringe peaks increases. And when  $g$  increases,  $m_1$  increases in the same proportion as evident from equation (2.11), causing the spacing between adjacent fringe peaks ( $l_2 - l_1$ ), to decrease almost with the same proportion. Note that Equation (2.15) can be generalized for the spacing between any two fringe peaks, not necessarily being adjacent to each other, and can be written as,

$$l_n - l_1 = \frac{2g}{m_1 m_n} = \frac{2g}{m_1(m_1 - n)}, \quad (2.16)$$

where  $m_n$  represents the number of full wavelengths the wave  $l_n$  ( $l_n > l_1$ ) travels before adding back in phase, and  $(n-1)$  is the number of fringe peaks in between  $l_1$  and  $l_n$ .

Now, to quantify the amount of chirp, lets assume a free space wavelength of value  $l_3$  ( $l_3 > l_2$ ) makes the fringe peak just adjacent to the fringe peak of  $l_2$ , then we can write, like Equation (2.15),

$$l_3 - l_2 = \frac{2g}{(m_1 - 1)(m_1 - 2)}. \quad (2.17)$$

Using Equation (2.15) and (2.17), we get the spacing difference of the non-uniform spacing of adjacent peaks as,

$$(l_3 - l_2) - (l_2 - l_1) = \frac{4g}{m_1(m_1 - 1)(m_1 - 2)}. \quad (2.18)$$

For the condition of fringe peak, as stated by equation (2.11), the parameter  $d$  of Equation (2.10) gets the value as,

$$d = \left( \frac{4pg}{1} + j_2 - j_1 \right) = 2mp, \quad (2.19)$$

where  $m$  is an integer, and putting this value of  $\delta$  in Equation (2.6), the value of the parameter  $q$  becomes zero. Thus for the wavelengths of the fringe peaks, Equation (2.10) can be written as,

$$V_c(l) = B\Re(l) f_s^2(l) \left\{ r_{pr} + t_{pr} f_a(g) \right\}^2 + G(m\lambda^2). \quad (2.20)$$

Similarly, for the condition of fringe troughs, the parameter  $\delta$  of Equation (2.10) must have the value as,

$$d = \left( \frac{4pg}{1} + j_2 - j_1 \right) = (2m + 1)p, \quad (2.21)$$

and putting this value of  $\delta$  in Equation (2.6), the value of the parameter  $q$  becomes again zero. And thus for the wavelengths of the fringe troughs, Equation (2.10) can be written as,

$$V_c(l) = B\Re(l) f_s^2(l) \left\{ r_{pr} - t_{pr} f_a(g) \right\}^2 + G(m\lambda^2). \quad (2.22)$$

Even if we ignore the Gaussian noise and assume that the responsivity characteristics of the photodiodes are independent of wavelengths, i.e.  $\Re(\lambda)$  is a constant, we may not find the intensity values of Equation (2.20) and (2.22) as the peaks and the troughs in the output of our linear array CCD spectrometer due to the modulation of the signal by the profile of the optical source  $f_s^2(l)$ . (Note, this is different than the limitation that the CCD elements can correspond only to discrete wavelengths). To find out the wavelengths of the fringe peaks and the troughs defined by Equations (2.19) and (2.21), in addition to filtering out the Gaussian noise, one must demodulate the signal response using the profile of the optical source being used for the system to undo the modulation effects, or must use an optical source which is perfectly white, i.e., the profile of the optical output is independent of wavelengths and is a constant. The achievement of a perfectly white optical source is not very practical yet, and the demodulation of the signal response using the profile of the optical source to undo the modulation effects, is not practical for real time applications due to the fact that the source intensity may vary over time and the profile may not follow a fixed curve (either analytic or numeric). When the optical source is Gaussian

but of pretty wide band, an estimate of the EFPI gap length  $g$  can be made though, by assuming the peaks of the modulated signal response as the fringe peaks, and troughs of the modulated signal response as the fringe troughs.

To filter out the Gaussian noise of the signal response of the wavelength modulated EFPI sensor system, a low-pass filter must be used. To find out the appropriate coefficients of the filter is very crucial, specially when the dynamic range of the EFPI gap variation is wide. When the EFPI gap is large, the spacing between the fringe peaks and/or troughs gets closer, and when the EFPI gap is small the spacing between the fringe peaks and/or troughs gets further, and the coefficients of the filter must be chosen after considering all these dynamic variations of the fringes. An adaptive filtering scheme, depending on the range of the EFPI gap, might be more appropriate in this purpose.

The precision of finding the wavelengths of fringe peaks and/or troughs, also depends on the wavelength spacing (in nm) between adjacent CCD elements of the linear array spectrometer, because the wavelengths of the actual peaks and troughs may not coincide to the calibrated wavelength values of the CCD elements. An interpolation scheme is helpful in this purpose to increase the precision of the wavelengths of the fringe peaks and/or troughs.

#### **2.4.2 FFT Method**

The frequency of the fringe pattern of the signal response of the wavelength modulated EFPI sensor system, though modulated by the profile of the optical source and a chirp, varies with the variation of the EFPI gap  $g$ . The fast Fourier transformation (FFT) method uses this variation of the frequency of the fringe pattern of the response to find out the EFPI gap length  $g$ . After implementing a high-pass filtering on the EFPI signal response, to filter out any DC value, a fast Fourier transformation is implemented on the filtered data. The ‘frequency’ bin having the maximum magnitude (i.e. the bin having the maximum energy) of the FFT transformation is

calibrated against the corresponding known EFPI gap length  $g$ , and applying this for a good number of EFPI gap lengths, the coefficients of a second order curve is found out which can transform (or curve fit) any bin value to the corresponding EFPI gap length. Applying a Gaussian interpolation technique [Shin92], or zero padding the data before doing the FFT, the resolution or accuracy of finding the EFPI gap can be increased by at least an order of magnitude.

The zero padding of the data before implementing the FFT, or the spectral interpolation after implementing the FFT, are in effect equivalent to the implementation of a window function on the data. Note that by taking a fixed length of data we are implicitly implementing a rectangular window on the data. A Hamming window, Hanning window, or a Blackman window can be implemented on the data if the energy of the sidelobe of the rectangular window needs to be reduced. The spectral resolution of the FFT depends on the length of the window being implemented.

For a simulated signal of 1024 element data having an EFPI gap of 50  $\mu\text{m}$  and signal-to-noise ratio (SNR) of 30 dB, the variance of the calculated gap is found to be 0.2089 for the FFT method, 0.0449 for the FFT method with Gaussian fit, 0.0475 for the FFT method with zero padding (the length of padded zeros being equal to the length of the data), and, 0.0138 for the FFT method with both Gaussian fit and zero padding.

Appendix C.2 provides the Matlab code for the implementation of the FFT method using Gaussian interpolation technique, and Figure 2.8 and 2.9 show the filtered data and the FFT magnitude values respectively, for the wavelength modulated EFPI sensor system, using the Ocean Optics S100 linear array spectrometer of SIE-687, and having an EFPI air gap of 80 micrometer.

Figure 2.8 is plotted as index of active elements versus intensity, not wavelength versus intensity. And as the wavelength spacing between adjacent CCD diode elements are not uniform, as depicted in Figure 2.10, the chirp of the EFPI gap is not well represented in Figure 2.8. The

chirp is corrupted due to the non-uniform wavelength spacing between adjacent CCD elements. Theoretically, this corruption of the chirp can be used to our advantage by placing the CCD elements in such a non-uniform spacing fashion that the chirp completely disappears from the plot of index of active elements versus intensity. In that case the output becomes simply an amplitude modulated single frequency signal, without having any chirp.

The FFT method of finding the EFPI gap  $g$ , though very fast for real-time applications, is not very precise, mainly may be due to its dependence on the curve fitting coefficients, which must be derived from a set of data associated with known EFPI gap values. A self-calibrated method which uses a special transformation, instead of FFT, can find the EFPI gap  $g$  with more precision and is presented below.

### 2.4.3 Discrete Gap Transformation Method

A special transformation, termed here as *discrete gap transformation* (DGT), based on the parameter  $\frac{4pg}{l}$  of Equation (2.2), is given as [Shin97],

$$I(g_m) = \sum_{n=1}^N x(n) \exp\left(j \frac{4pg_m}{l(n)}\right), \quad (2.23)$$

where  $x(n)$  are the intensity sequence of the elements of the linear array CCD spectrometer,  $l(n)$  are the wavelengths corresponding to the elements,  $g_m$  is any EFPI gap length, and  $N$  is the total number of active elements in the CCD spectrometer (which is 1024 in our wavelength modulated EFPI sensor system). To get the square of the magnitude of the DGT transformation, using Equation (2.23), we get,

$$|I(g_m)|^2 = \left| \sum_{n=1}^N x(n) \cos\left(\frac{4pg_m}{l(n)}\right) \right|^2 + \left| \sum_{n=1}^N x(n) \sin\left(\frac{4pg_m}{l(n)}\right) \right|^2. \quad (2.24)$$

For any given set of acquired data with an EFPI gap of  $g$ , the magnitude of the DGT transformation of Equation (2.24) is maximum when  $g_m$  equals  $g$ . As in the discrete Fourier

transformation (DFT) where the transform magnitude is the maximum at the frequency which corresponds to the dominating frequency of the data set, in the DGT transformation the transform magnitude is the maximum at the gap which corresponds to the gap of the data set. Thus for any given data set to find out the associated EFPI gap, we find the magnitude of the DGT transformation for a discrete set of values (with an incremental step of our expected precision) of  $g_m$ , and the value for which the transformation magnitude is the maximum is the EFPI gap. Appendix C.3 includes the Matlab code for finding the EFPI gap for any set of data, acquired from a wavelength modulated EFPI sensor system, using the DGT method, and Figure 2.11 shows the magnitude of DGT of 11 sets of data, acquired with the wavelength modulated EFPI sensor system with a nominal EFPI gap of 50 micrometer and increasing the gap by 1 micrometer at each step. Note that, there are about couple of micrometer of offset between the nominal values and the calculated ones. The existence of this offset might be due to two reasons, first, the nominal value of the EFPI gap was set using a micro translation stage which might not be very accurate, and second, the DGT method may have a fixed offset from the actual EFPI gap based on the parameters of the system. But note that the step increase of the EFPI gap of 1 micrometer are very precisely measurable by the DGT method.

Figure 2.12 shows the calculated EFPI gap using the FFT method and the DGT method, both using the same 7 sets of data acquired from the wavelength modulated EFPI sensor system with the same nominal EFPI gap of about 50 micrometer. For all the 7 data sets, every parameter of the system is the same, the only difference is the noise. The relative precision of the DGT method is very obvious from the Figure.

Though the DGT method is precise, it is very computation intensive. As the EFPI gap can be of any value in the range 30 micrometer to 300 micrometer, to find out the gap for a given data set with a desired precision of say 1 nanometer, one must calculate the DGT magnitude using the Equation (2.24) starting with a value of  $g_m$  of 30 micrometer and then increasing it by one nanometer at each step until 300 micrometer, entailing the computation of Equation (2.24) for 270,000 times, which is unrealistic for real-time applications, specially when one finds that the

*sine* and *cosine* functions of Equation (2.24) need to be evaluated  $N$  (and in our case 1024) times for every iteration of calculation of Equation (2.24). To reduce this burden of computation for real-time applications we present below a way which dramatically decreases the number of iterations, but still uses the DGT method [Shin97].

#### **2.4.4 FFT and then Discrete Gap Transformation with Golden Search Rule**

As depicted in Figure 2.11, the magnitude of the DGT transformation is very much like a Gaussian curve having only one peak. To use this monotonicity of the magnitude of the DGT transformation to our advantage, we apply a peak search method rather than calculating Equation (2.24) at fixed increments of  $g_m$ . A peak search method named *golden search rule* [Press88], is applied to find the value of  $g_m$  for which the magnitude of the transformation is the maximum, as coded in function *vFindTruGap()* of Appendix A. The iteration of calculation of Equation (2.24) is further reduced by reducing the range of the EFPI gap to be searched, by first making a rough estimate of the EFPI gap using the FFT method, which is pretty fast. The range of the EFPI gap to be searched, is assumed the EFPI gap found from the FFT method plus/minus 5  $\mu\text{m}$ . And such, for the same precision of 1 nanometer, the iteration of calculation of Equation (2.24) is reduced to only about 20, rather than 270,000 as stated earlier. The real-time application of the DGT method is thus now made very feasible.

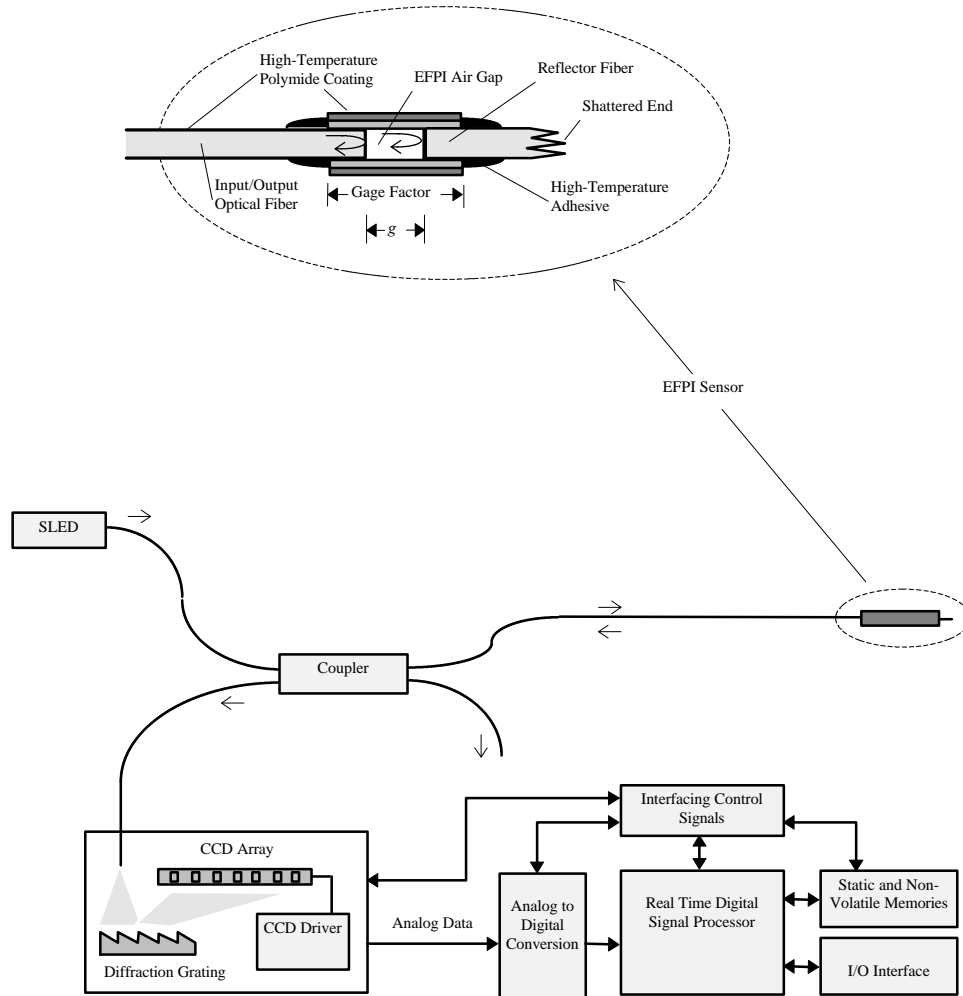


**Figure 2.1**

Construction of the real-time wavelength modulated EFPI sensor system.

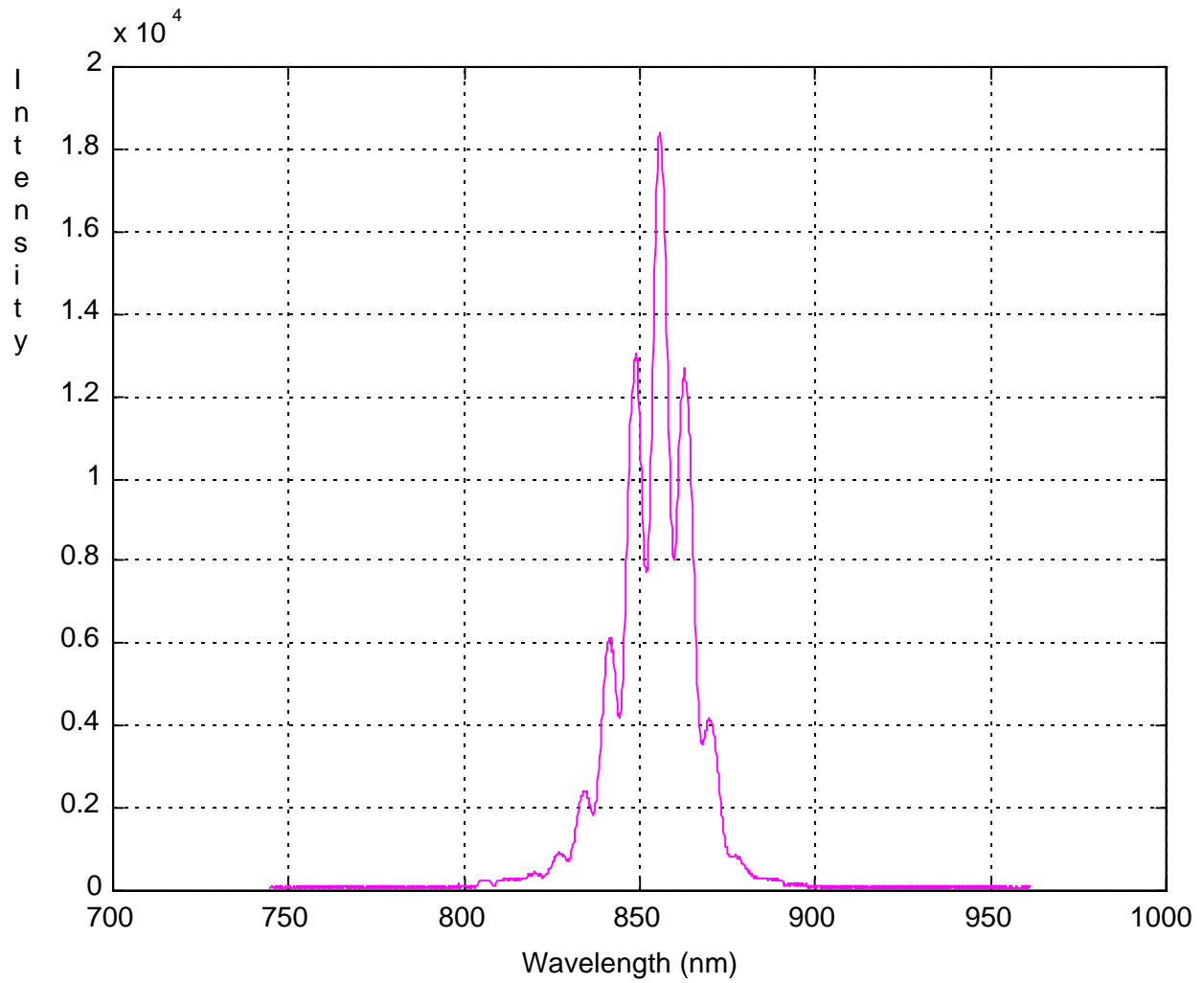


**Figure 2.2**

Signal response of the wavelength modulated EFPI sensor system with the Ocean Optics S1000 linear array spectrometer of SIE-687, and an EFPI gap of 50.0 micrometer.

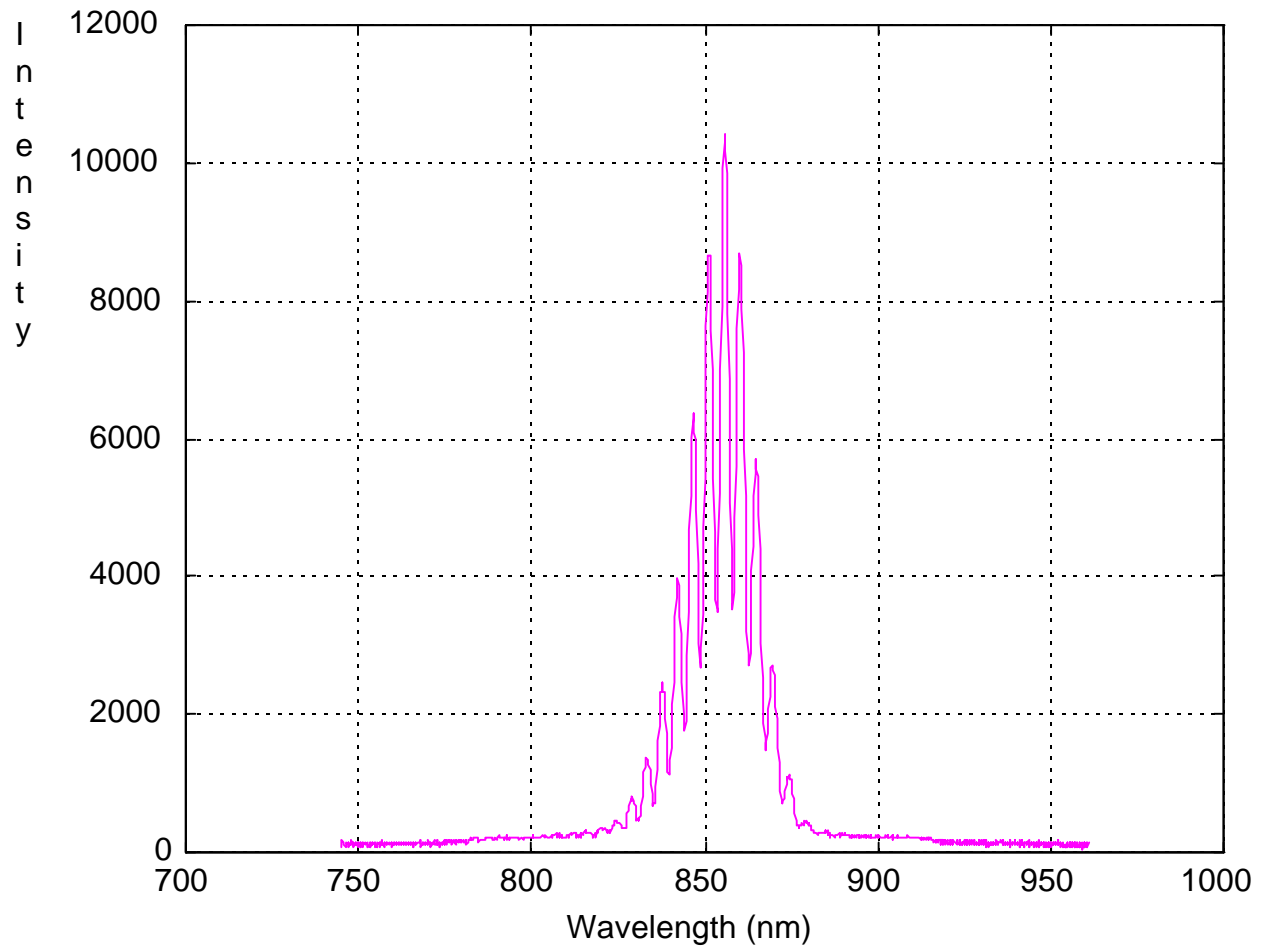
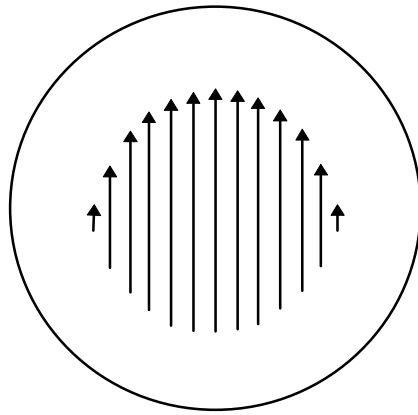


**Figure 2.3**

Signal response of the wavelength modulated EFPI sensor system with the Ocean Optics S1000 linear array spectrometer of SIE-687, and an EFPI gap of 80.0 micrometer.



HE<sub>11</sub>, the lowest-order mode

**Figure 2.4**

Electric field distribution across the cross-section of the single-mode fiber.

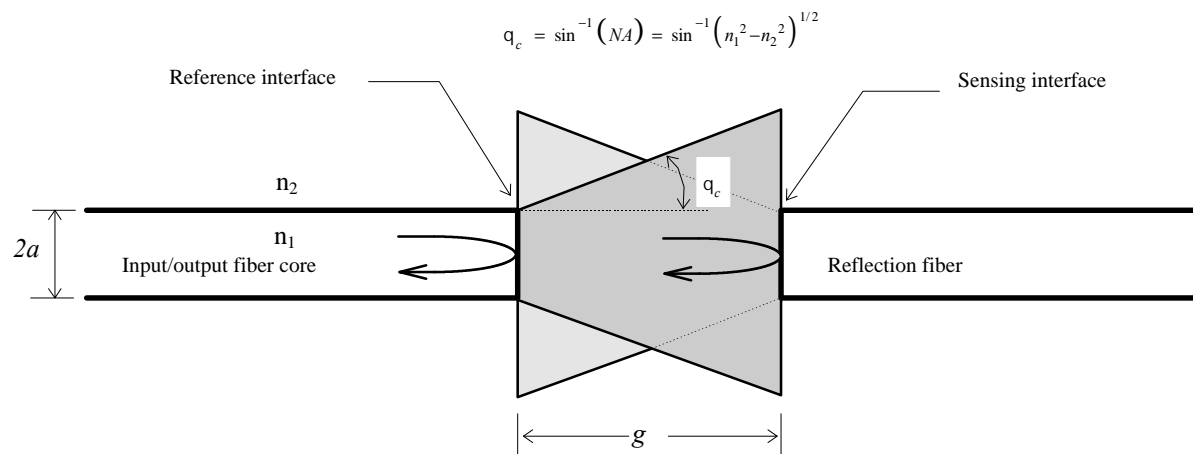


**Figure 2.5**

Loss effect in coupling the optical power back into the input/output fiber after the reflection at the sensing interface.

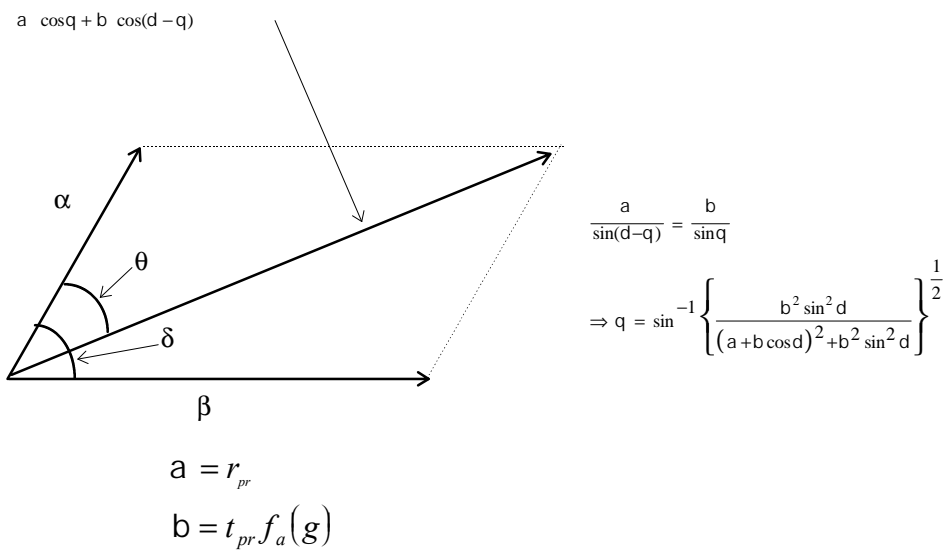


**Figure 2.6**

Phasor addition of two waves of amplitude  $\alpha$  and  $\beta$  having the same frequency and a difference of phase of  $\delta$ .

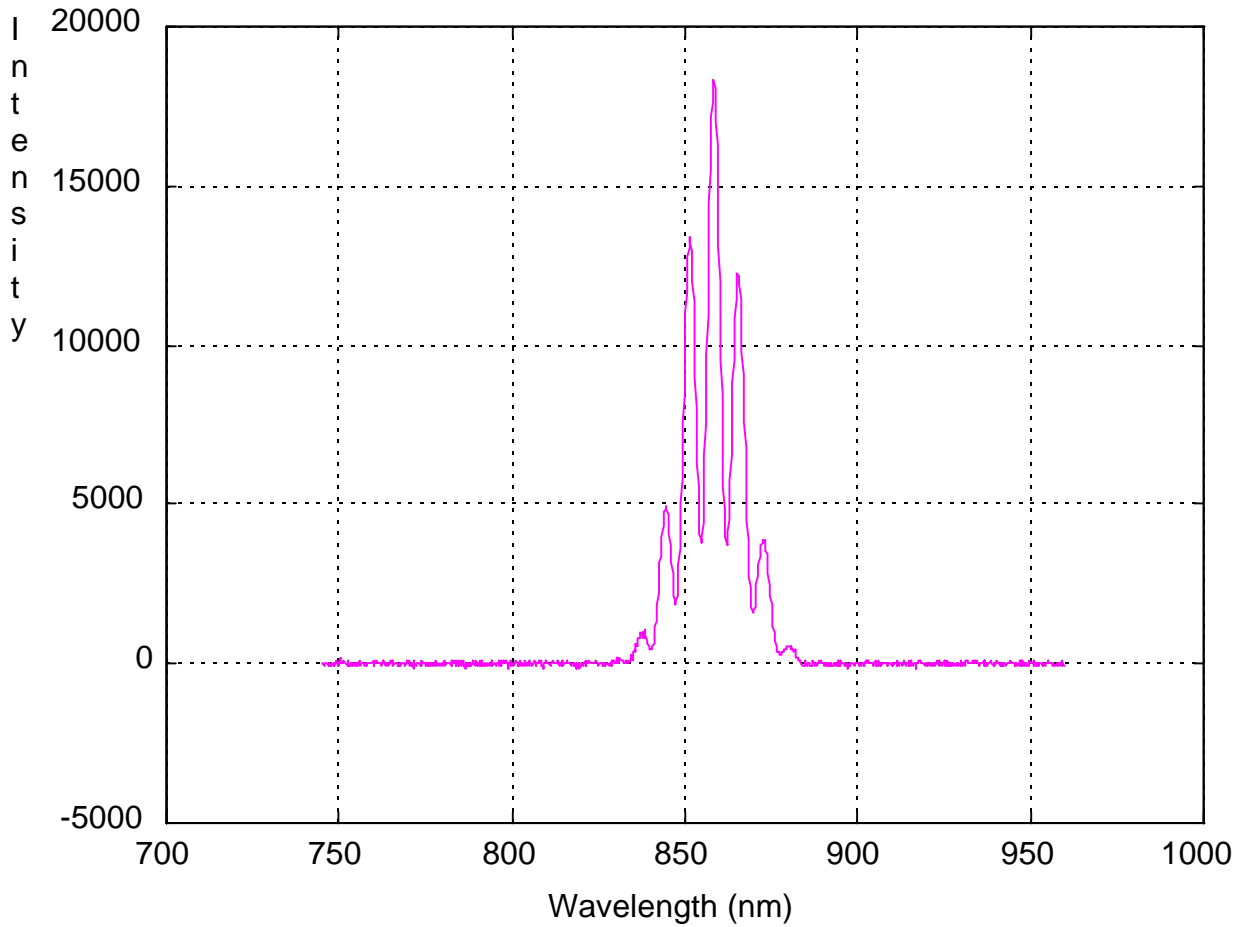


**Figure 2.7**

Simulated signal response of the wavelength modulated EFPI sensor system model for an EFPI gap of 50.0 micrometer and other parameters as given in Appendix C.1.

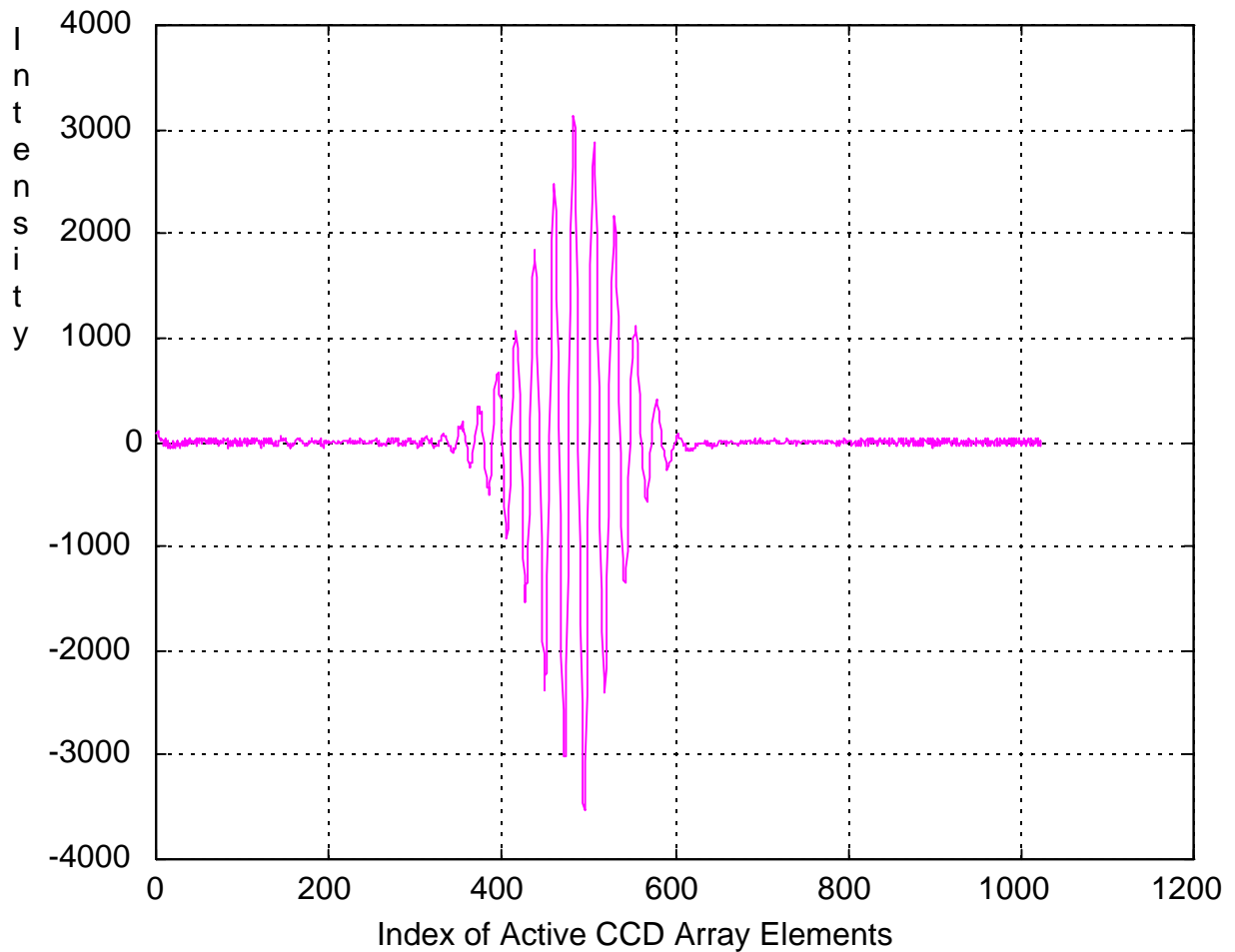


**Figure 2.8**

The filtered data of a wavelength modulated EFPI sensor system, which uses the Ocean Optics S1000 linear array spectrometer of SIE-687, and has an EFPI air gap of 80.0 micrometer. The filter used is of high-pass Butterworth of order 3 and of normalized cutoff frequency of 0.03.

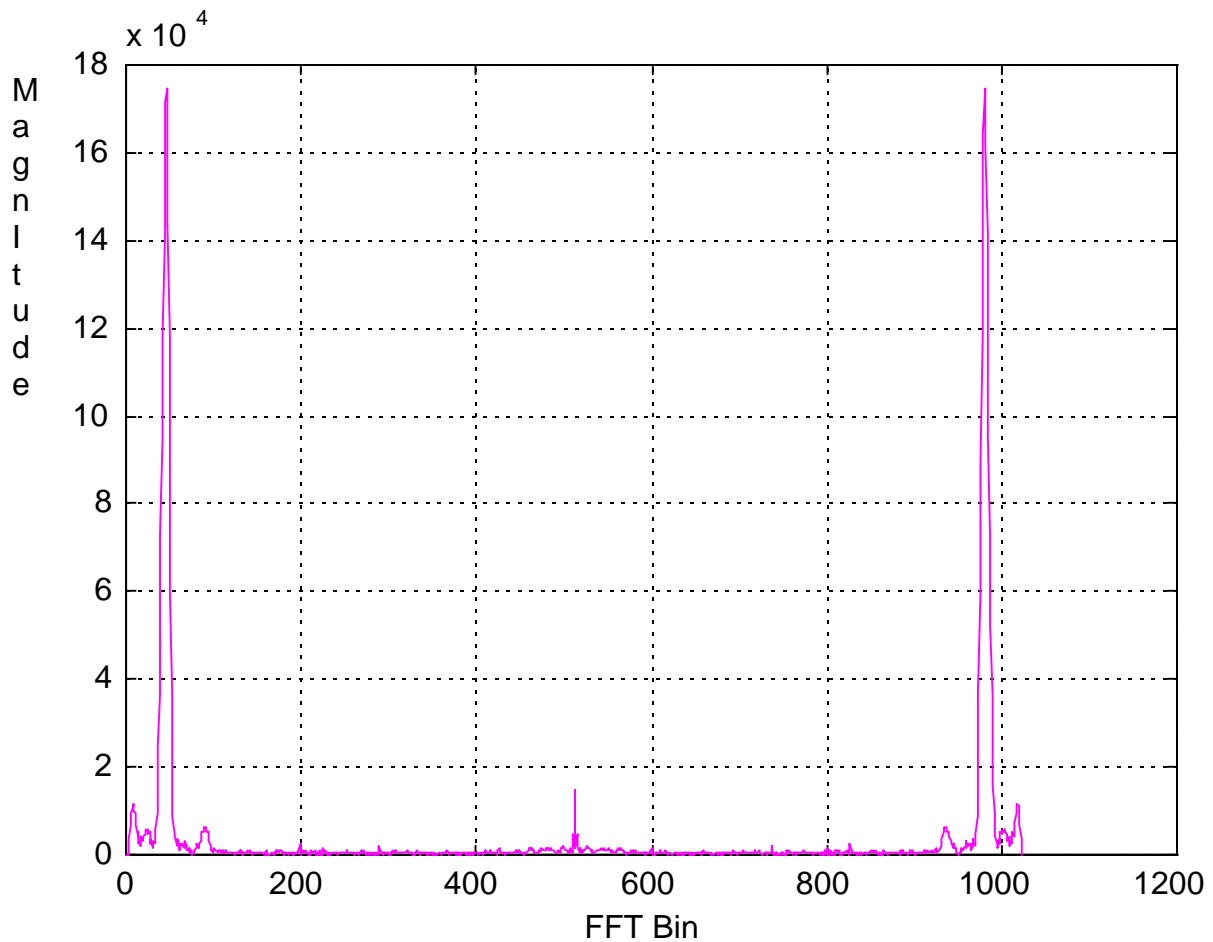


**Figure 2.9**

The FFT implementation on the filtered data of a wavelength modulated EFPI sensor system, which uses the Ocean Optics S1000 linear array spectrometer of SIE-687, and has an EFPI air gap of 80.0 micrometer.

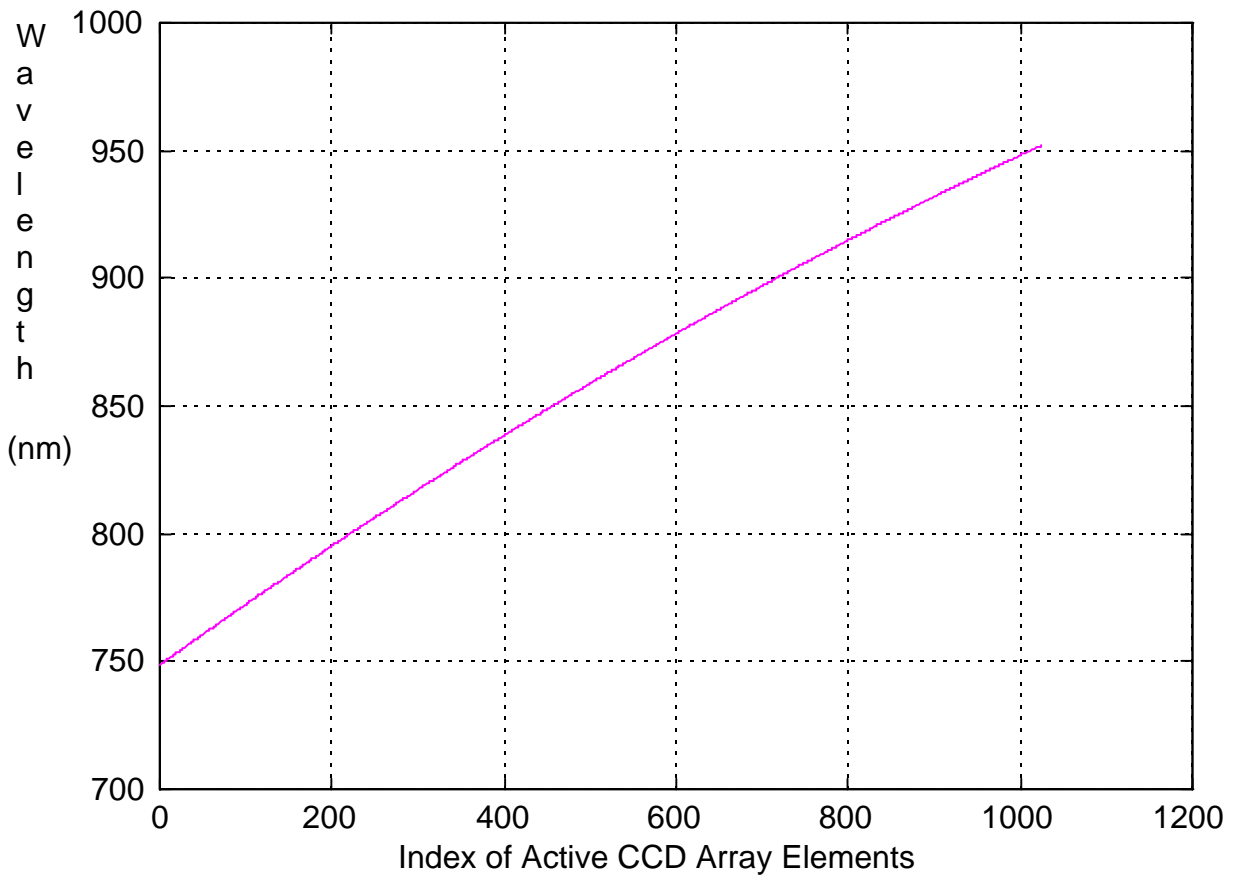


**Figure 2.10**

Index of the 1024 active elements, of the Ocean Optics S1000 linear array spectrometer of SIE-687, versus their corresponding wavelengths. Note that the curve is not linear due to non-uniform spacing in wavelengths between adjacent elements.

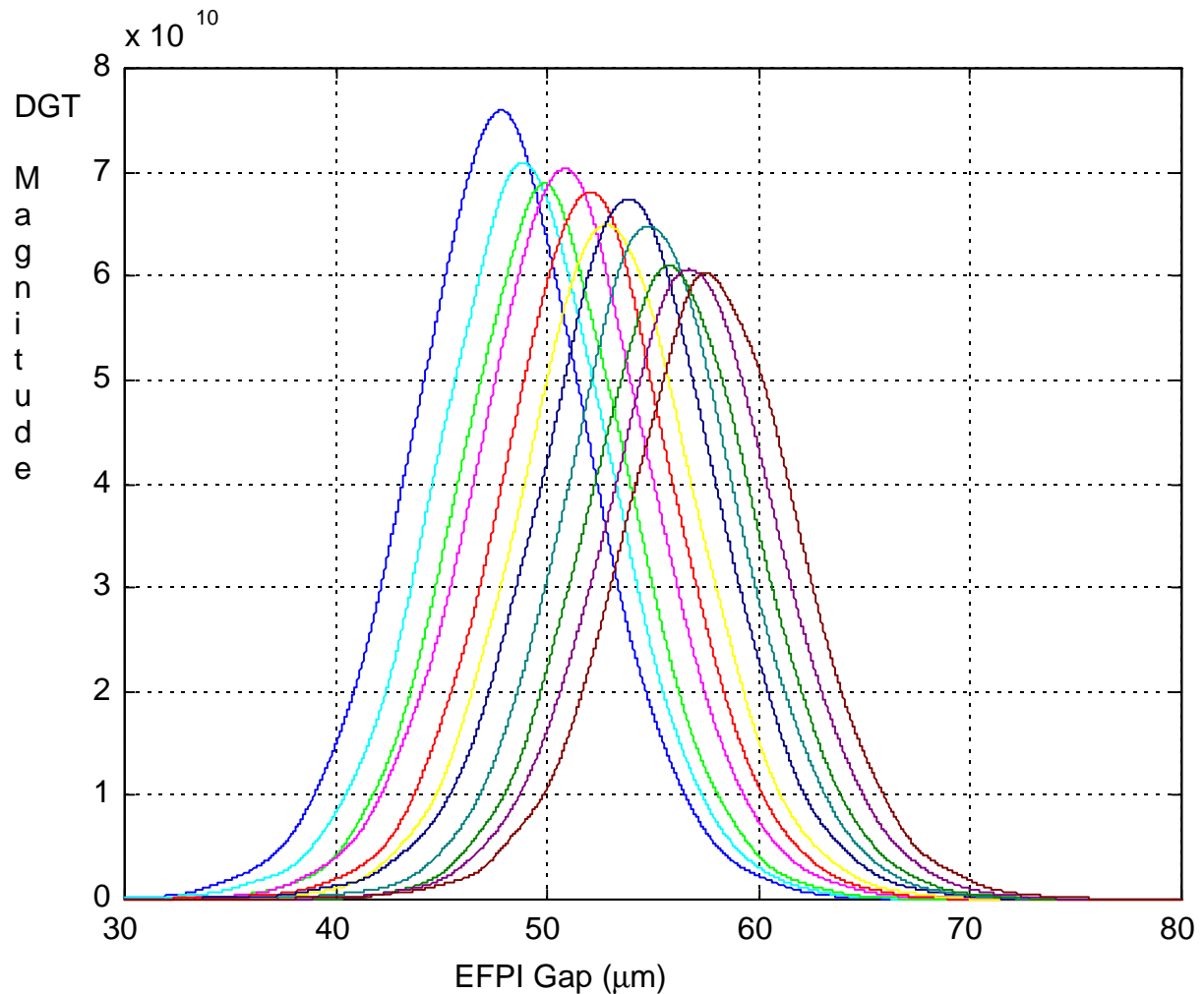


**Figure 2.11**

Magnitude of discrete gap transformation (DGT) of 11 sets of data, acquired with the wavelength modulated EFPI sensor system with a nominal EFPI gap of 50 micrometer and increasing the gap by 1 micrometer at each step. The system uses the Ocean Optics S1000 linear array spectrometer of SIE-687. Note that, there are about couple of micrometer of offset between the nominal values and the calculated ones.

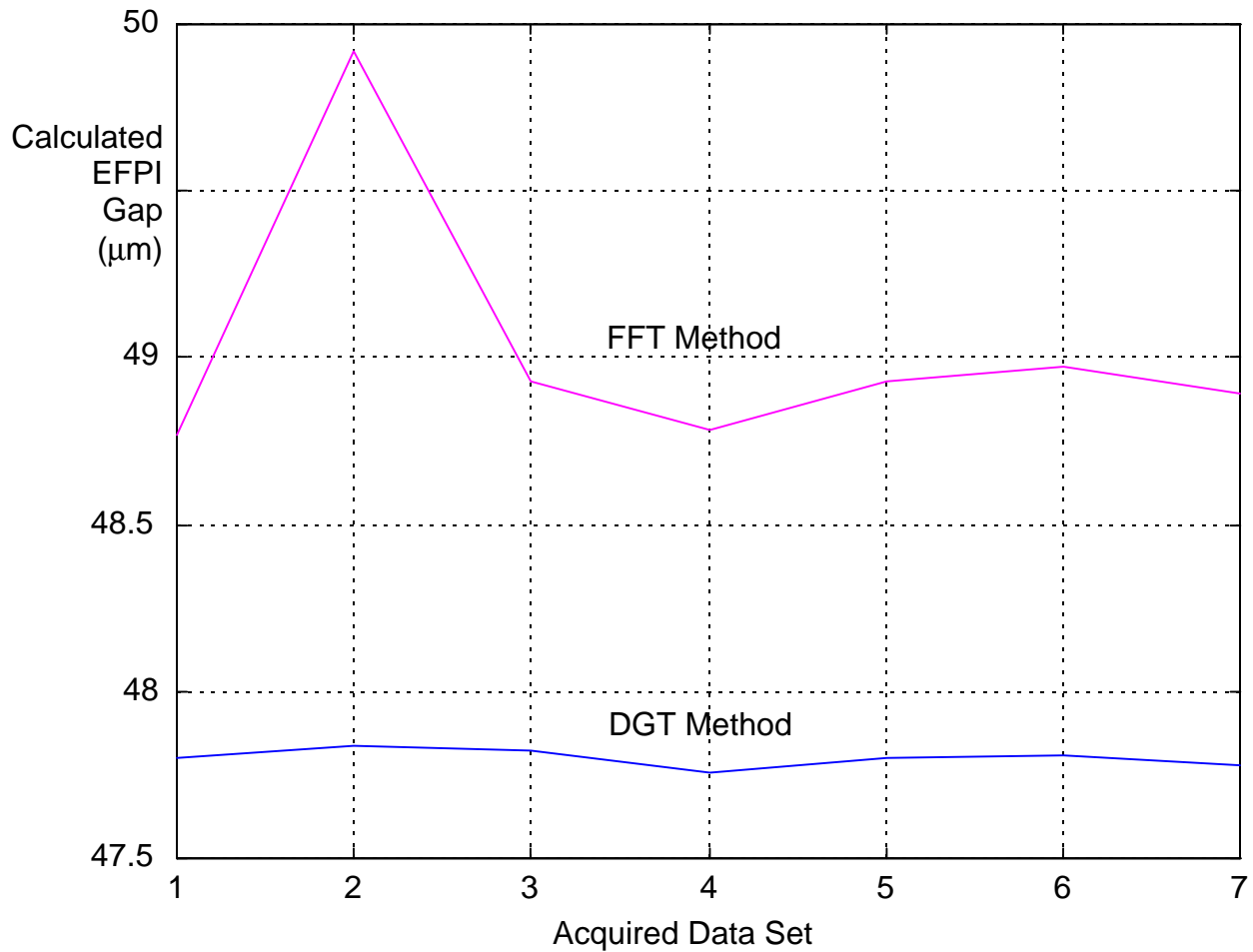


**Figure 2.12**

Calculated EFPI gap using the FFT method and the DGT method, both using the same 7 sets of data acquired from the wavelength modulated EFPI sensor system with the same nominal EFPI gap of about 50 micrometer, using the Ocean Optics S1000 linear array spectrometer of SIE-687. For all the 7 data sets, every parameter of the system is the same, the only difference is the noise. Note the relative precision of the DGT method compared than that of the FFT method.

## Chapter 3

### The FBG and the LPG Sensor Systems

Fiber Bragg Grating (FBG) sensors and Long-Period Grating (LPG) sensors are very suitable for multiplexed and/or distributed operations. Though both the FBG and LPG sensors are fabricated by writing periodic variations of refractive index along the axis of the fiber, there are fundamental differences in the theory of operations of these sensors. In this chapter we develop the real-time system constructions of these sensors, and present their signal responses, their theory of operations, and their real-time signal processing techniques.

#### 3.1 Construction and Signal Response of the FBG Sensor System

Figure 3.1 shows the construction of the real-time FBG sensor system. A broadband optical source of super luminescent light-emitting diode (SLED) is used to couple light into a single-mode optical fiber. The light propagates to the FBG sensors through an optical coupler, the wavelengths resonating with the index gratings, written along the axis of the fiber sensors, reflect back and propagate in the reverse direction through the same coupler to reach to the end of a fiber and to hit on a reflection diffraction grating, which separates the light components by diffracting different wavelengths at different angles on to a CCD array. The CCD array senses the intensity of different wavelength components of the light at different elements. The discrete analog pulses of the CCD array elements are digitized and transferred to the digital signal processing (DSP) unit, which finds out in real time the peak wavelengths of the reflected waves which corresponds to each Bragg sensor. For any Bragg sensor the amount of shift in the wavelength of the reflection peak from its nominal value, determines the amount of perturbation

inflicted on the sensor. For multiplexed sensor systems, as shown in Figure 3.1, the dynamic range of the wavelength shift of any sensor must not overlap with the dynamic range of the wavelength shift of any other sensors, to avoid confusion which reflection peak belongs to which sensor. Note that the multiplexed sensors can be inserted at any physical distances along the fiber arm, and at any order (i.e., any sensor can have any reflection wavelengths), but they must have different reflection wavelengths with non-overlapped dynamic range of wavelength shifts. Any measurable perturbation localized at any sensor of the multiplexed system, shifts the corresponding reflection peak only.

Figure 3.2 shows the signal response of an FBG sensor system with two sensors multiplexed on the same fiber, one having a reflection wavelength of 852.6 nm and the other with a reflection wavelength of 862.3 nm. The figure shows that the intensity value of the reflection peak of one sensor is much higher than that of the other, this is due to couple of reasons. First, each Bragg sensor is unique in fabrication and has its own reflection characteristics. Second, the optical output profile of the SLED source usually has a Gaussian shape and hence has different intensity for different wavelengths. Note that any tensile strain inflicted on a Bragg sensor shifts the wavelength of the reflection peak towards higher wavelengths, and any contractile strain shifts the wavelength of the reflection peak towards lower wavelengths.

### **3.2 Construction and Signal Response of the LPG Sensor System**

While in the case of the FBG sensor system the signal of interest is the reflection spectrum from the sensors, the signal of interest for the LPG sensor system is rather the transmission spectrum from the sensors, because in the LPG technique the wavelengths resonating with the index grating pattern couples into the cladding modes to be lost instead of reflecting back through the fiber. Figure 3.3 shows the construction of a real-time LPG sensor system. A broadband optical source of super luminescent light-emitting diode (SLED) is used to couple light into a single-

mode optical fiber. The light propagates through the LPG sensors to reach to the end of the fiber and to hit on a reflection diffraction grating, which separates the light components by diffracting different wavelengths at different angles on to a CCD array. The CCD array senses the intensity of different wavelength components of the light at different elements. The discrete analog pulses of the CCD array elements are digitized and transferred to the digital signal processing (DSP) unit, which finds out in real time the transmission loss wavelength peaks which corresponds to each LPG sensor. For any LPG sensor the amount of shift in the wavelength of the transmission loss peak from its nominal value, determines the amount of perturbation inflicted on the sensor. For multiplexed sensor systems, as shown in Figure 3.3, the dynamic range of the wavelength shift of any sensor must not overlap with the dynamic range of the wavelength shift of any other sensors, to avoid confusion which transmission loss peak belongs to which sensor. Note that the multiplexed sensors can be inserted at any physical distances along the fiber arm, and at any order (i.e., any sensor can have any transmission loss wavelengths), but they must have different wavelengths of transmission loss peaks with non-overlapped dynamic range of wavelength shifts.

Figure 3.4 shows the signal response of a single LPG sensor. Note that there are several dips in the transmission spectrum, each dip corresponding to the coupling of the fundamental guided mode to a different cladding mode. Due to these multiple dips in the transmission spectrum, the multiplexing of the LPG sensors are bit more complicated than that of FBG sensors. Like an FBG sensor, any tensile strain inflicted on an LPG sensor shifts the wavelength of the transmission loss peaks towards larger wavelengths, and any contractile strain shifts the wavelength of the transmission loss peaks towards smaller wavelengths.

### **3.3 Fabrication of the FBG and the LPG Sensors**

Both the FBG and the LPG sensors are fabricated by ‘writing’ periodic refractive index gratings (or index variations) along the axis of the optical fiber. Typically the index grating periods for an

LPG sensor is in the order of hundreds of micrometers, while that of an FBG sensor is only in the order of one micrometer. Unjacketed hydrogen loaded germanosilicate optical fibers are exposed to UV radiation of wavelengths 244-248 nm through an optical mask with the required index grating periods. For the FBG sensors the index gratings can also be written by exposing the unjacketed fiber to a spatial interference fringe pattern of the UV laser source. The conditions of exposure, i.e., the laser power, the duration of the exposure, and the length and type of the mask, if used, are different for different types of sensors and are discussed in references [Veng96, Grat95, Jone95]. After writing the index grating with the UV source, the sensor must be annealed to stabilize its optical characteristics. The environments of the annealing process depend on the fiber and the grating type, the operating temperature of the sensor, and the required stability of the sensor [Veng96]. The sensors we used, were fabricated by F&S Inc., Blacksburg, Virginia.

### 3.4 Principle of Operations of the FBG and the LPG Sensor Systems

Both the FBG and the LPG sensing techniques work on the principle of mode coupling. But there are fundamental differences between the two techniques, and that is, in the case of Bragg grating the forward propagating mode couples with the reverse propagating mode of the fiber core, and in the case of long period grating the forward propagating mode of the core couples with the forward propagating mode of the cladding and eventually gets lost due to high attenuation of the cladding modes.

The fraction of power,  $P(z)$ , coupled from a mode of propagation constant  $b_1$  to a mode of propagation constant  $b_2$ , in an interaction length of  $z$  is given as [Hill90, Grat95],

$$P(z) = \frac{|k|^2}{|k|^2 + \left(\frac{d}{2}\right)^2} \sin^2 \left[ z \left( |k|^2 + \left(\frac{d}{2}\right)^2 \right)^{\frac{1}{2}} \right], \quad (5.1)$$

where  $k$  is the coupling coefficient between the two modes, and  $d$  is the detuning parameter given as,

$$d = b_1 - b_2 - 2qp / \Lambda , \quad (5.2)$$

where  $q$  is an integer and  $\Lambda$  is the period of index grating. Note that in Equation (5.1), the complete transfer of power from one mode to the other is not possible without equating the detuning parameter  $d$  to zero, which is a special condition and termed as phase matching condition. Applying phase matching condition we get,

$$\Lambda = \frac{2qp}{b_1 - b_2} = \frac{2qp}{\Delta b} . \quad (5.3)$$

It is obvious from equation (5.3) that, if the differential phase propagation constant  $\Delta b$  is decreased by a factor, the period of index grating must be increased by the same factor to hold the phase matching condition.

Figure 3.5 shows the phase matching conditions of mode coupling for both the FBG and the LPG sensors. For a single-mode fiber, the propagation constant of the forward propagating fundamental mode,  $b_{01}$ , must satisfy the condition,

$$n_2 \frac{2p}{\lambda} < b_{01} < n_1 \frac{2p}{\lambda} , \quad (5.4)$$

to remain guided along the length of the fiber [Keis91], where  $n_1$  and  $n_2$  are the refractive indices of the core and the cladding, respectively, and  $\lambda$  is the free space wavelength of any particular frequency of our wide-band SLED optical source that remains guided along the fiber. For the case of Bragg or short period gratings, of single-mode fiber, the mode coupling occurs from the forward propagating fundamental mode, having the propagation constant  $b_{01}$ , to the reverse propagating fundamental mode, having the propagation constant  $-b_{01}$ . So the differential propagation constant  $\Delta b$  equals  $2b_{01}$ , which is large, as shown in Figure 3.5 (a), resulting short grating periodicity. And the phase matching condition for Bragg gratings of single-mode fiber can then be written as,

$$\Lambda = \frac{qp}{b_{01}}. \quad (5.5)$$

Note that, there can only be a single value of wavelength that can satisfy Equation (5.5) for a fixed value of  $\Lambda$  and  $q$ .

For the case of long period gratings, of single-mode fiber, the mode coupling occurs from the forward propagating fundamental mode, having the propagation constant  $b_{01}$ , to the forward propagating cladding modes having the propagation constant  $b_{cl}^n$ , where  $n$  is the order of the cladding mode. So the differential propagation constant  $\Delta b$  equals  $(b_{01} - b_{cl}^n)$ , which is small, if compared to  $2b_{01}$  as shown in Figure 3.5 (a), resulting long grating periodicity. And the phase matching condition for long period gratings of single-mode fiber can then be written as,

$$\Lambda = \frac{2qp}{b_{01} - b_{cl}^n}. \quad (5.6)$$

Cladding modes are also known as leaky modes, and they must have a propagation constant less than the value of the cutoff condition, which is  $n_2 \frac{2p}{\lambda}$  [Keis91]. Note that, for a fixed value of  $\Lambda$  and  $q$ , for each order of cladding mode there is a different value of wavelength which can satisfy Equation (5.6), creating different transmission loss peaks for a single sensor. This is unlike FBG sensors, where only a single reflection peak is created per sensor.

With the change of any measurable perturbation on the FBG or the LPG sensor, the pattern or period of the refractive index grating ( $\Lambda$ ) of the sensor is changed, which basically shifts the wavelength for which the phase matching condition is satisfied. Note, that the propagation constant of the fundamental mode is different for different wavelengths which are guided into our single-mode fiber from the SLED source. The wavelengths for which the phase matching condition is satisfied are the reflection peaks for the case of the FBG sensors, and are the transmission loss peaks for the case of the LPG sensors. By calculating the amount of this phase

matching wavelength shifts, one can find the amount of perturbing measurables, which causes the shifts.

### 3.5 Demodulation Techniques for the Signal Response of the Real-Time FBG Sensor System

The wavelength of the Bragg reflection peaks change with the change of the measurable perturbation inflicted on the corresponding sensor. The signal processing scheme must find out this wavelength shift of each sensor,  $\Delta\lambda_B$ , from the nominal peak wavelength of the Bragg reflection,  $\lambda_B$ , in real-time. Once the  $\lambda_B$  and the  $\Delta\lambda_B$  is found for any sensor, the longitudinal strain  $\epsilon$  applied on the sensor can be calculated as [Grat95],

$$e = \frac{\Delta\lambda_B}{\lambda_B(1 - p_e)}, \quad (5.7)$$

where  $p_e$  is the photo elastic coefficient, and is of value 0.22 for germanosilicate fibers.

Bragg grating sensors are also sensitive to change of temperature,  $\Delta T$ , and the relationship is given as [Jone95],

$$\Delta T = \frac{\Delta\lambda_B}{\lambda_B(a + \chi)}, \quad (5.8)$$

where  $a$  is the coefficient of thermal expansion which is  $0.55 \times 10^{-6}$  for silica, and  $\chi$  is the fiber thermo-optic coefficient and is  $8.3 \times 10^{-6}$  for germanosilicate glass. Note that as the temperature sensitivity of a Bragg grating sensor primarily depends on the thermo-optic coefficient of the fiber, by controlling the amount of thermo-optic dopants of the fiber, the thermal sensitivity of the sensor can be controlled.

The signal response of our real-time fiber Bragg grating sensor system, as shown in Figure 3.2, has the intensity of the reflected wave at discrete 1024 wavelengths, which correspond to the

1024 elements of the CCD spectrometer. As we do not have continuous wavelength response, the actual wavelength of the peak reflection can be in-between two adjacent discrete wavelength values. Moreover, the shape of the Bragg reflection peaks are not very well defined in many cases, due to imperfection in fabrication processes, and such the range of each reflection peak may spread over a wide range of wavelengths with an undefined shape. Considering these factors, an energy centroid method is used in determining the wavelength of the peak reflections of each sensor, which improves both the resolution and the accuracy of the peak wavelength, if compared to the discrete wavelength just having the maximum intensity. In the centroid method, the wavelength of peak reflection,  $\lambda_p$ , is calculated as [Shin97],

$$\lambda_p = \frac{\sum \lambda_i P_i}{\sum P_i}, \quad (5.9)$$

where  $\lambda_i$  is the wavelength of the  $i$ 'th pixel of the CCD array, and  $P_i$  is the corresponding optical intensity. The centroid must be calculated over the range of the Bragg reflected signal only. This is performed first by searching the discrete wavelength having the maximum intensity within the dynamic range of the Bragg sensor, and then calculating the energy moment starting at a predetermined number of pixel left to the maximum intensity pixel and ending at a predetermined number of pixel right from the maximum intensity pixel. The predetermined numbers are decided for each individual sensor, by using an optical spectrum analyzer and finding where the Bragg reflected signal drops to 95% of the peak value.

An interpolation scheme, instead of the centroid method, can also be implemented to improve the resolution in determining the wavelength of the peak reflection. Without the implementation of either the centroid method or any interpolation scheme, the resolution of the system will be too crude. For example, if the CCD spectrometer has a minimum wavelength spacing of 0.4 nanometer between adjacent CCD elements, for a nominal peak wavelength of a Bragg reflection of 800 nanometer, using Equation (5.7) we get an approximate resolution of 640  $\mu\epsilon$  for strain, which might be too high for many applications.

### **3.6 Demodulation Techniques for the Signal Response of the Real-Time LPG Sensor System**

For a wide-band signal response of each LPG sensor, there are several dips in the transmission spectrum, each dip corresponding to the coupling of the fundamental guided mode to a different cladding mode. For the real-time signal processing purposes, it is only necessary to track the movement (in wavelength) of only one transmission dip per LPG sensor. Due to several transmission dips per LPG sensor the real-time implementation of the multiplexed sensors is very difficult than that of FBG sensors. For multiplexed LPG sensors one must make sure, that the transmission dip being tracked by the signal processing software, must not be confused with other transmission dips, if any, that may appear within the dynamic range of the tracked transmission dip.

Usually the deepest transmission loss peak, of a particular LPG sensor, should be tracked to find its shift in wavelength to measure the amount of measurable that perturbs the optical index grating of the real-time LPG sensor.

### **3.7 Summary of the FBG and the LPG Sensor Systems**

In this chapter we develop the real-time system constructions of the FBG and the LPG sensors, and present their signal responses, their theory of operations, and their real-time signal processing techniques. From the hardware point of view, the real-time construction of the FBG and the LPG sensor systems are exactly the same as of the wavelength modulated EFPI sensor systems, which we dealt in details in Chapter 2. The signal processing techniques of the FBG and the LPG sensor systems are not as computationally intensive as that of the EFPI systems. We presented a centroid method to improve the accuracy in locating the reflectance peak for the case of an FBG sensor, and the transmission loss peak for the case of an LPG sensor.

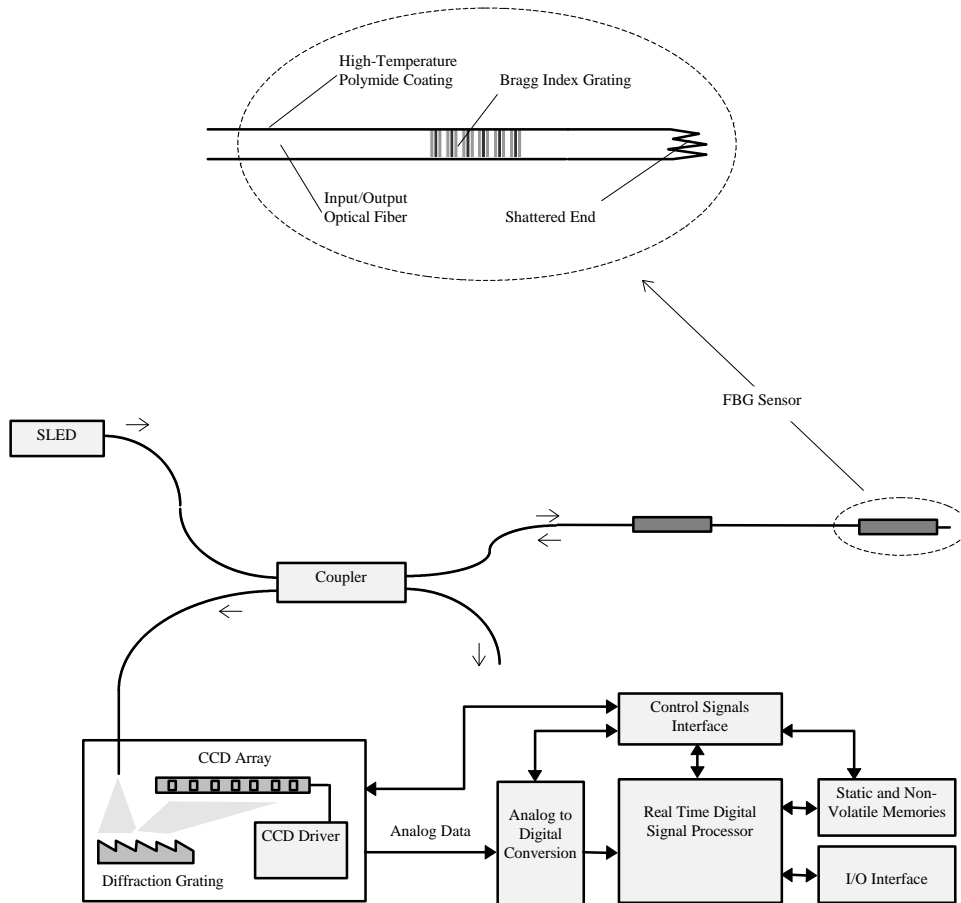


**Figure 3.1**

Construction of a real-time FBG sensor system. The system shows two sensors multiplexed on the same fiber, but having different reflection frequencies.

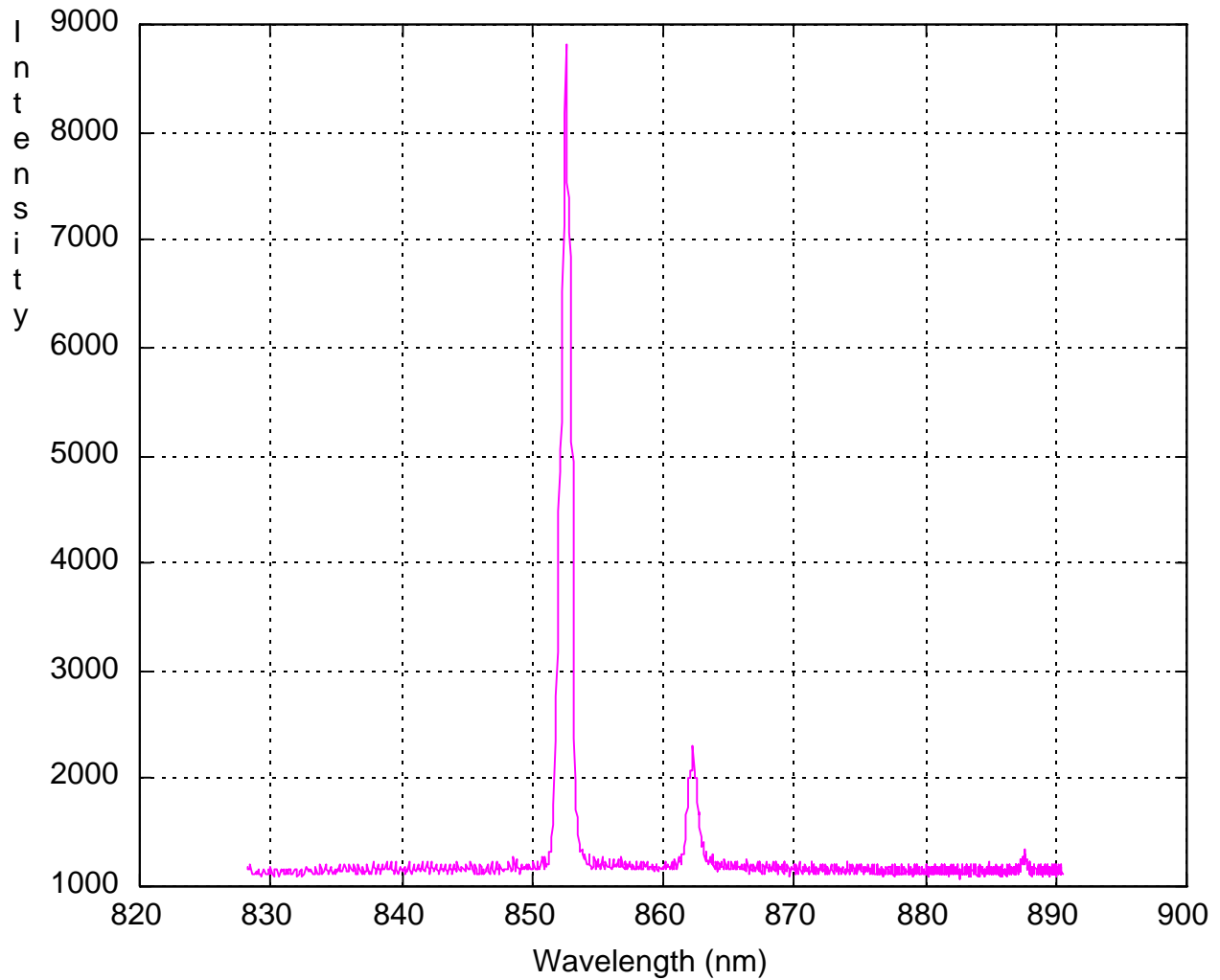


**Figure 3.2**

Signal response of an FBG sensor system with two sensors multiplexed on the same fiber. One sensor has a reflection wavelength of 852.6 nanometer and the other has a reflection wavelength of 862.3 nanometer.

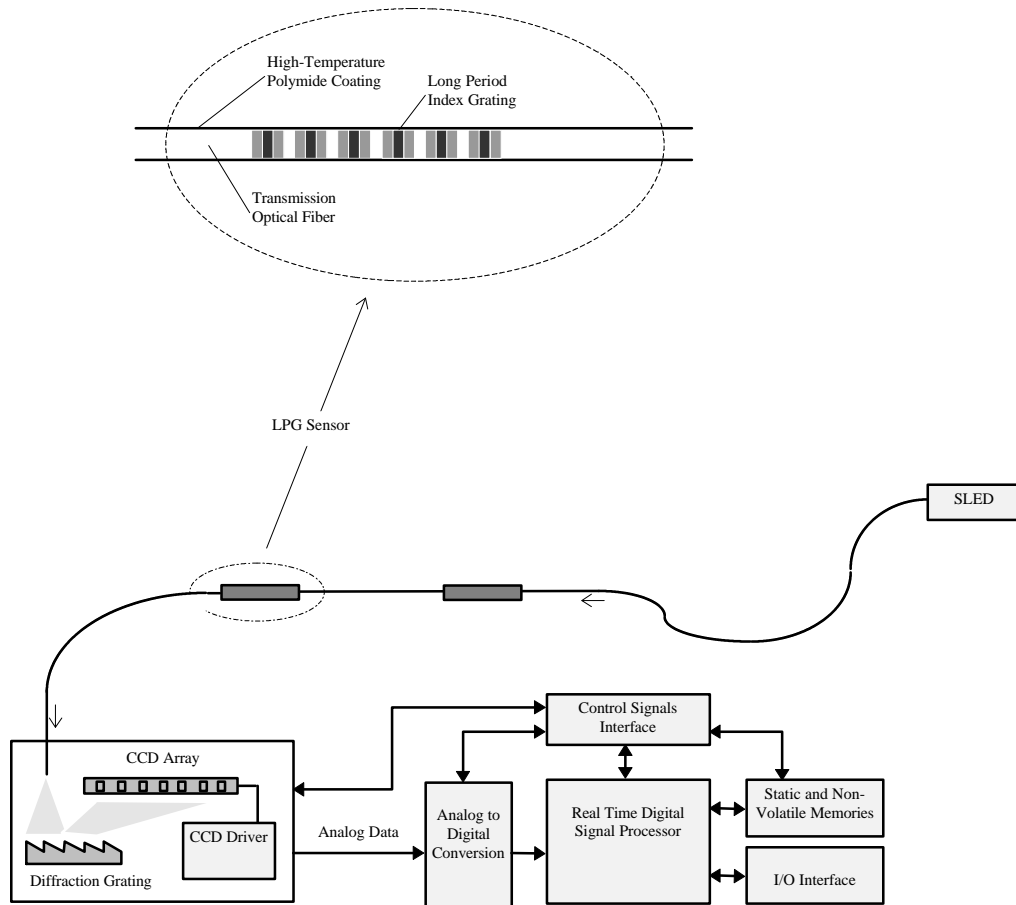


**Figure 3.3**

Construction of a real-time LPG sensor system. The system having two sensors multiplexed on the same fiber, but with different transmission loss frequencies.

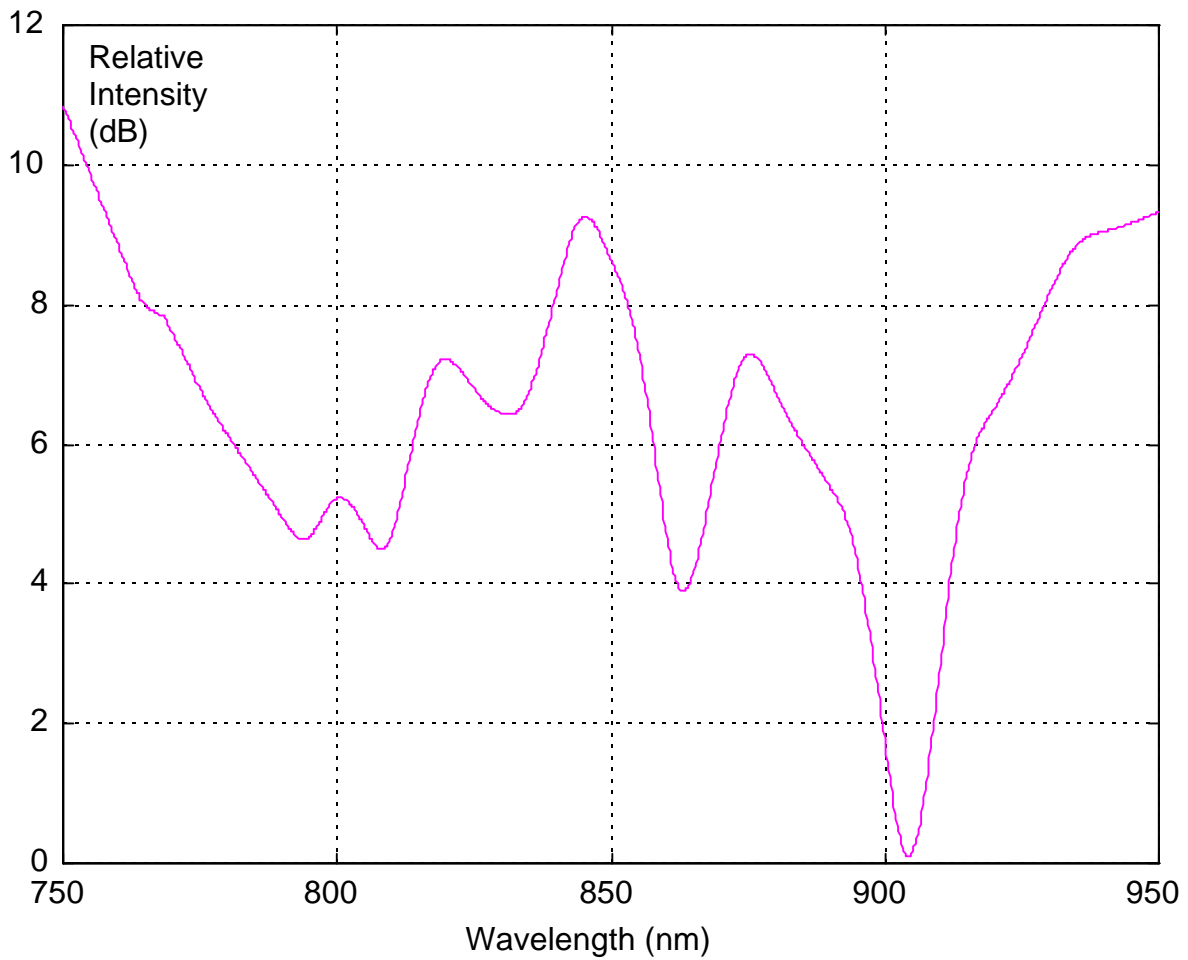


**Figure 3.4**

Signal response of an LPG sensor. Note that, there are several dips in the transmission spectrum, each dip corresponds to the coupling of the fundamental guided mode to a different cladding mode. The intensity in dB is shown relative to the highest transmission loss in the spectrum.

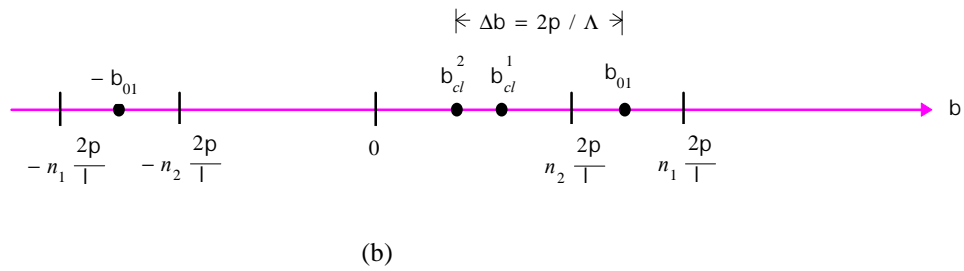
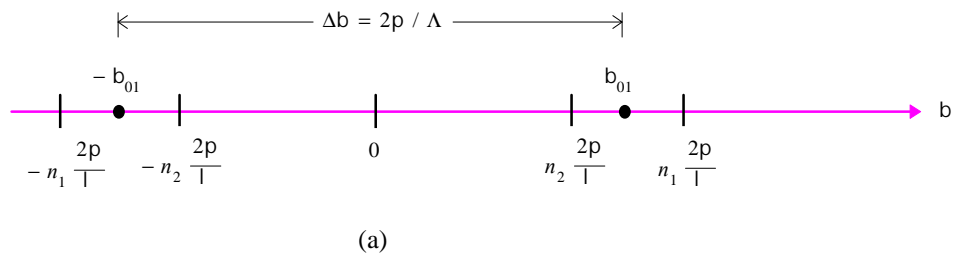


**Figure 3.5**

Phase matching conditions of mode coupling for (a) Bragg or short period gratings, and (b) long period gratings [Veng96]. The smaller the differential phase propagation constant  $\Delta\beta$ , the longer the period of gratings  $\Lambda$ .

## Chapter 4

### Hardware Development

All the hardware is designed and developed for the stand alone wavelength modulated optical fiber sensor system. The system is capable of digitizing and processing all the signals in real time. All the components and functions of the hardware system are discussed in this chapter.

#### 4.1 S1000 Linear Array CCD Spectrometer

Figure 4.1 shows the picture of an S100 linear array spectrometer of Ocean Optics, Inc. [OCEA93], which is used for diffracting (with reflection diffraction gratings) the optical frequency components, of the fiber sensor, at different angles and collecting the corresponding optical intensities to a linear CCD array. Each element or pixel of the CCD array corresponds to a particular optical frequency. The S100 has a maximum clock input rate of 2 MHz. The video output pin of the S1000 sequentially outputs 1100 CCD pixel voltages in analog pulses, at half the input clock rate, with a range of 0 to 10 volts (added with a user selective offset), at intervals of 8192 input clock pulses. At the beginning of each integration period, all pixel charges are transferred at once to CCD registers for sequential read out through the video output pin. After the transfers, the photodiodes continue to conduct again, and charge is stored proportional to the light intensity over the integration period. An enable input signal allows to output triggers, synchronized with the 1100 analog video output pulses, which is at half the rate of the input clock frequency. The rising edge of the trigger pulses are used as the conversion triggers for the analog-to-digital conversion of the 1100 analog video output pulses.

Of the 1100 digitized data points, the first 14 data points are the measure of the analog baseline. The next 1030 data points are the photodiode readings of which the first 2 and the last 4 are ineffective diodes, thus making it a 1024 element CCD. The rest of the data points are electrical zeros.

## 4.2 Analog-to-Digital Conversion Board

An analog-to-digital conversion board, as shown in the picture of Figure 4.2, is designed and developed. The analog-to-digital conversion (ADC) board interfaces the CCD spectrometer with the TMS320C40 board. It digitizes the pulse amplitude signals from the spectrometer using the conversion trigger pulses, also coming from the spectrometer. The ADC board converts the analog pulses, each pulse corresponding to a particular CCD element and hence representing the intensity of a particular optical frequency, into 12-bit parallel digital signals which are interfaced with the communication ports of the TMS320C40 (henceforth also known as just 'C40) DSP chip. The interfacing connections are as shown in Figure 4.3. There are six communication ports in the 'C40 chip, and each port can handle 8 parallel data bits. For parallel interfacing of our 12-bit data we need two communication ports of the 'C40 chip, Figure 4.3 shows the interfacing with the Port 3 and 4. Note that after reset, the communication Ports 3, 4, and 5 are configured as input ports, and the communications Ports 1, 2, and 3 are configured as output ports [Texa93]. A token forcing circuit is provided, if necessary, in the ADC board, which is required for an output port to be configured as an input port, or vice versa. For the data acquisition and processing advantages, the 12-bit data of the ADC board is read as 16-bit data by the 'C40 chip, the least significant 4 bits being always zero (i.e. grounded). As the speed of the 'C40 chip is very high (40 MHz) if compared to the speed of the ADC chip (800 kHz), only a one way handshaking is implemented for transferring data from the ADC board to the 'C40 communication ports.

The Burr-Brown 12-bit analog-to-digital converter, ADS7810, is used for the ADC board. A brief description of this analog-to-digital converter is provided below.

#### *Analog-to-Digital Converter ADS7810:*

The speed of the Ocean Optics' S1000 spectrometer allows an analog-to-digital converter no faster than 1 MHz. After extensive vendor search the most suitable ADC chip, for interfacing with the TMS320C40 communication ports, was decided to be 28-pin Burr-Brown CMOS 12-bit parallel converter, ADS7810, which is specified at 800 kHz sampling rate, having an industry standard  $\pm 10$  V analog input voltage range and a power dissipation under 250 mW [Burr93].

Though a 16-bit ADC were more appropriate for our system, a suitable chip did not exist at the time of our design with a sampling rate of around 1 MHz.

### **4.3 TMS320C40 Board**

A real-time signal processing board, named the TMS320C40 board, as shown in Figure 4.4, is designed and developed. The 'C40 board is the mother board of our sensor system. This board hosts the Texas Instrument's TMS320C40 (or just 'C40) floating point digital signal processor, which is used as the main processor for real time signal processing of the wavelength modulated optical fiber sensor system. The JTAG (or Boundary Scan) interface of the 'C40 chip is used to debug and/or upload/download programs to memory. The 'C40 board has a universal asynchronous receiver/transmitter (UART) to connect the system to any computer using the RS232 communication ports . The RS232 connection is used for the TCP/IP server in any computer to get access to the sensor system so that the server can send the sensor data in real-time if requested by any TCP/IP client through the Internet. The RS232 connection can also be used for any general purpose operations like uploading/downloading programs to/from the sensor

system, or running a small operating system for the sensor system from any host computer. 128K of 32-bit words of Non-volatile SRAM and 512K of 32-bit words of fast SRAM is provided on the 'C40 board. The non-volatile RAM keeps the system programs and data intact at power off, and such the system can run by itself at power on. The SRAM can be used for running programs faster as it has a very small access time. A watchdog timekeeper is provided which keeps track of time, and can be used to time stamp any data if required, or to put an interrupt to the 'C40 processor at any predetermined time intervals. Xilinx field-programmable gate arrays are used as programmable glue logic for timing and interfacing all the components of the 'C40 board. A brief description of all the major components of the board are given below.

*TMS320C40 DSP Processor:*

325-pin grid array TMS320C40 of Texas Instruments, a 32-bit RISC architecture floating point DSP processor [Tms93], is used as the main processor for our wavelength modulated optical fiber sensor system. Our processor has a speed rating of 40 MHz, i.e. 50-ns instruction cycle times. The 'C40 processor has an instruction set of 145 instructions, the instruction set being especially well suited to digital signal processing and other numeric-intensive applications. Most of the instructions take only a single cycle to execute. The floating point instructions are implemented using 12 (R0-R11) 40-bit wide extended-precision registers. Another 8 (AR0-AR7) 32-bit wide auxiliary registers are used primarily for address generation. Both the extended-precision and auxiliary registers can also be used as general purpose 32-bit integer registers.

The 'C40 processor has two identical data (32-bit wide) and address (31 bit wide) buses, termed global and local buses, which support shared memory systems. It has a JTAG interface for IEEE Boundary Scan and other standard connections. 512 byte of instruction cache and 8 K-byte single-cycle dual access program or data RAM are provided as on-chip memory in the 'C40 processor.

The 'C40 processor has six bi-directional communications ports and a six-channel DMA coprocessor for concurrent I/O and CPU operations. Separate internal data, program, and DMA coprocessor buses support parallel data, program, and I/O operations.

#### *UART PC16550D:*

44-pin PC16550D universal asynchronous receiver/transmitter (UART) with FIFOs of National Semiconductor [Nati95], is used with the 'C40 board for interfacing the stand alone real-time signal processing system with any serial communication ports of computers. The PC16550D performs parallel-to-serial conversion on data characters received from the CPU, and serial-to-parallel conversion on data characters received from any peripheral device or any MODEM. It has all the modem control functions, CTS, RTS, DSR, DTR, RI, and DCD. The CPU is capable of reading the status of the UART (e. g., the error conditions, and the type and conditions of the transfer), at any time of operation. It can generate and detect even, odd, or no parity, and can add or delete start, stop, and parity bits. The UART can generate a programmable baud rate ranging from DC to 1.5M baud, and is capable of handling 5-, 6-, 7-, or 8-bit characters.

#### *SRAM $\mu$ PD434008 and Nonvolatile SRAM DS1245:*

512K-word by 8 bits CMOS fast static RAMs  $\mu$ PD434008LE-20 [Stat95], of NEC Electronics Inc., are used to design 512K of 32-bit words of SRAM memory. The chips have a small plastic package of 36 pin. They have a very fast access time of 20-ns maximum.

128K x 8-bit nonvolatile static RAMs DS1245 of Dallas Semiconductor [Dall95a], are used to design 128K of 32-bit words of nonvolatile memory. It has direct interface with the 'C40 exactly like fast SRAM. Each nonvolatile SRAM has a self-contained lithium energy source, which automatically protects the data in the memory whenever the external power is turned off. It has 10 years minimum data retention capability in the absence of external power, and has unlimited write cycles with an access time of 70-ns.

#### *Watchdog Timekeeper DS1286:*

Watchdog timekeeper DS1286 of Dallas Semiconductor [Dall95b], is used as watchdog timer, to keep track of time, or to time-stamp any data, if required. It keeps track of hundredths of seconds, seconds, minutes, hours, days, date of the month, months, and years, and can generate separate interrupts at any programmable time intervals and/or when the watchdogged processor goes out of control. It has an embedded lithium battery source which has a greater than 10 years of timekeeping in the absence of any external source.

#### *Xilinx FPGA X C4003A:*

Two of the Xilinx field-programmable gate arrays (FPGAs) X'C4003A-4PC84 [Xilin94], are used to generate, buffer, and interface the control signals of the 'C40 processor, the PC16550D UART, and the memory devices. The X'C4003A-4PC84 is a 84-pin PLCC package with approximate gates count of 3000 and flip-flops count of 360 in a 10 x 10 configurable logic block (CLB) matrix. These FPGAs are configured by loading a binary file in it, and have unlimited reprogrammability. The X'C4003A chips provide programmable input pull-up or pull-down resistors, and programmable output slew rates. The X'C4003A can handle up to 24-mA sink current per output.

## **4.4 Programming the Logic for the Xilinx FPGA XC4003A-4PC84**

The base package of the Xilinx Foundation Series 6.0.1 software is used to program the logic of the FPGAs. The programming of the logic can be implemented by using VHDL or by using schematic capture from the library provided with the Foundation package. The schematic capture method is used for programming the Xilinx FPGAs as the logic required for our system is simple. Figure 4.5 and Figure 4.6 shows the schematics of the logic which are implemented in the Xilinx FPGAs. Once the schematic is drawn and a library for the schematic components is built, the Foundation software performs full automatic partitioning, placement, and routing of the

FPGA available resources to implement the logic. The software finally produces a *.bit* file which when loaded into the FPGA, the chip gets programmed as the logic of the schematic. The software has the provision of pre-selecting pins for specific signals

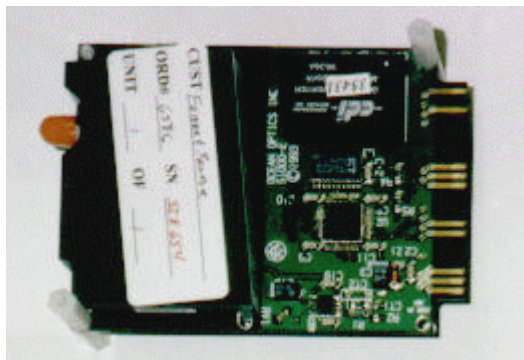


**Figure 4.1**

S1000 Linear CCD Array Spectrometer of Ocean Optics, Inc. (The card-edge connects to a set of 12-pin headers on the ADC board using a 44-pin card-edge connector and a ribbon cable.)

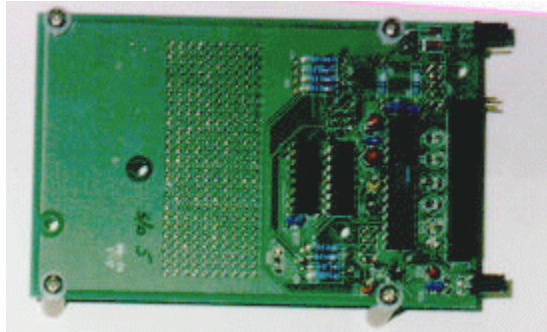


**Figure 4.2**

The analog-to-digital conversion (ADC) board. (A 32-pin socket, located on the back-side of the ADC board, directly connects to a set of 32-pin headers, on the back-side of the 'C40 board.)

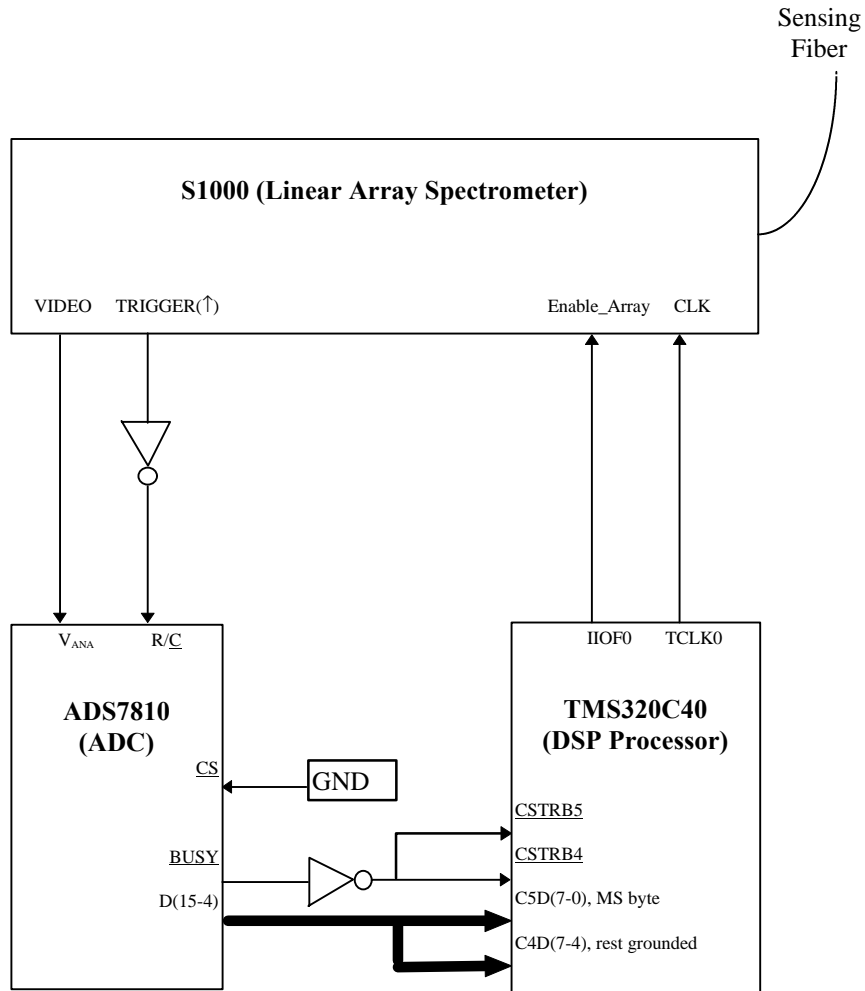


**Figure 4.3**

Interface connections of the CCD Spectrometer, the ADC chip, and the TMS320C40 chip.

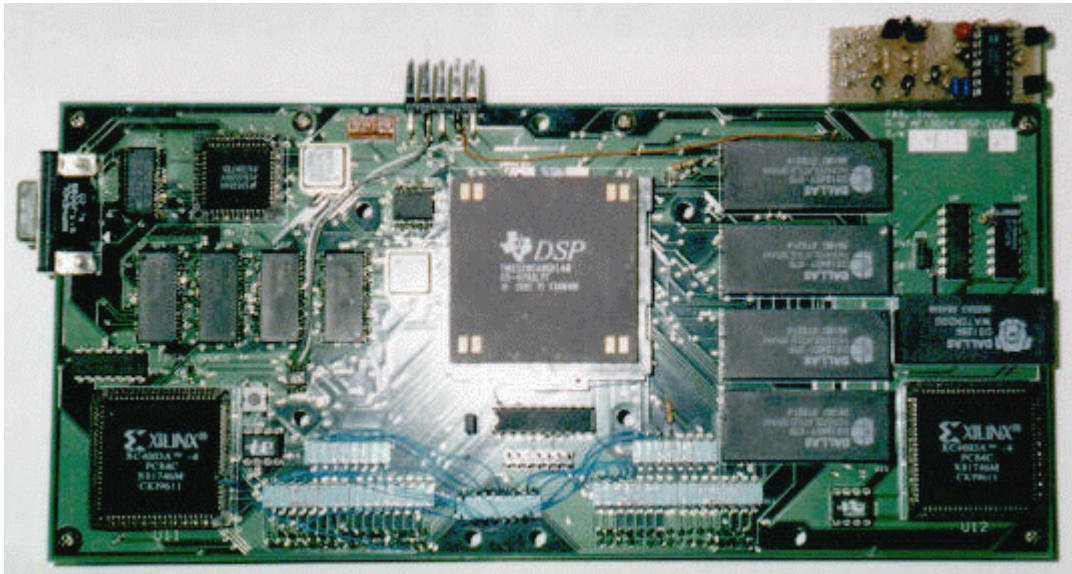


**Figure 4.4**

The TMS320C40 real-time signal processing board, which holds the 'C40 processor, the UART, SRAM, non-volatile SRAM, watchdog timekeeper, and the Xilinx FPGAs.

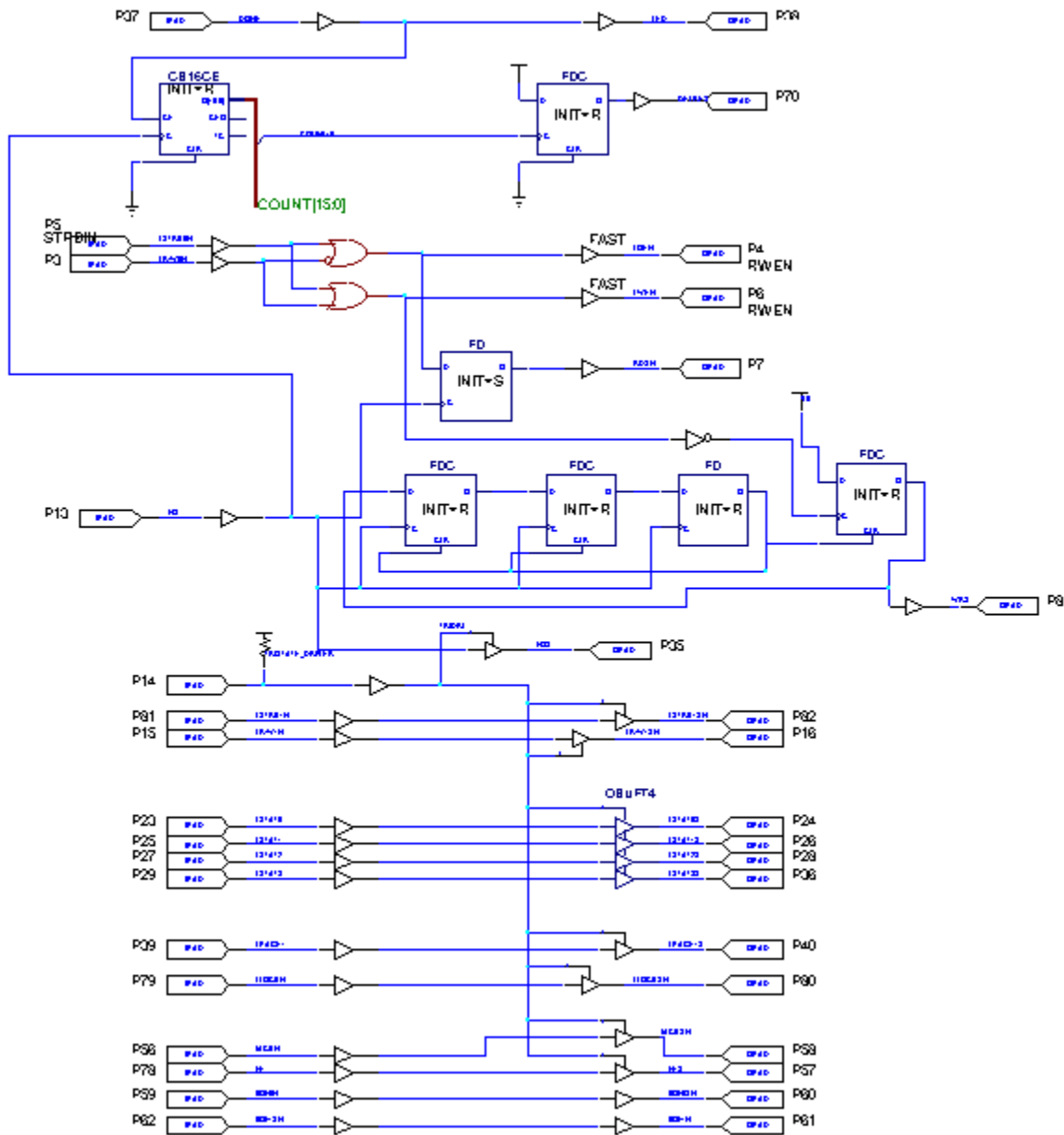


**Figure 4.5**

Top level schematic of the programmed logic for the Xilinx FPGA XC4003A-4PC84 to generate, buffer, and interface the control signals of the 'C40 local buses, the PC16550D UART, and the SRAM memory devices.

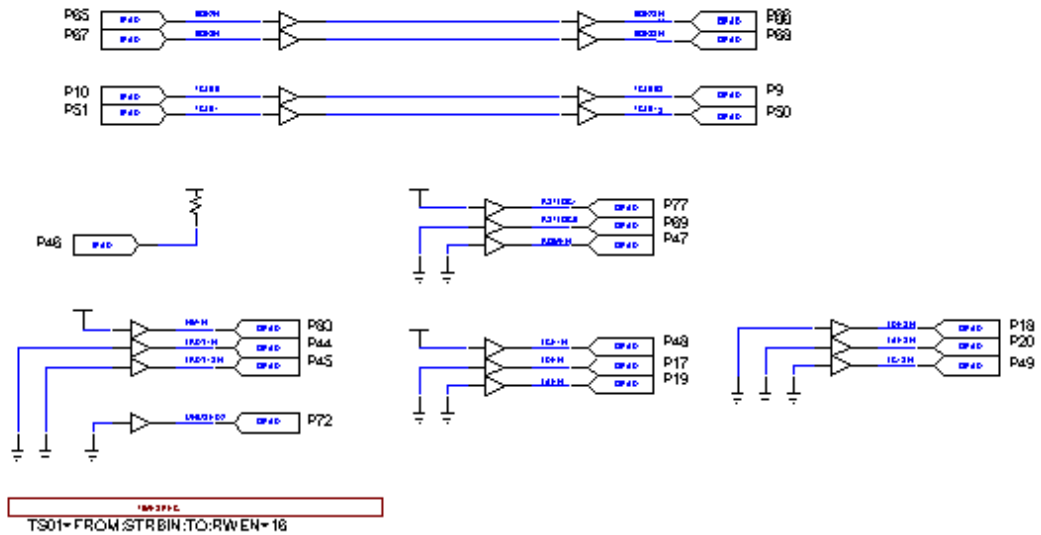


**Figure 4.5 (Cont d)**

Top level schematic of the programmed logic for the Xilinx FPGA XC4003A-4PC84 to generate, buffer, and interface the control signals of the 'C40 local buses, the PC16550D UART, and the SRAM memory devices.

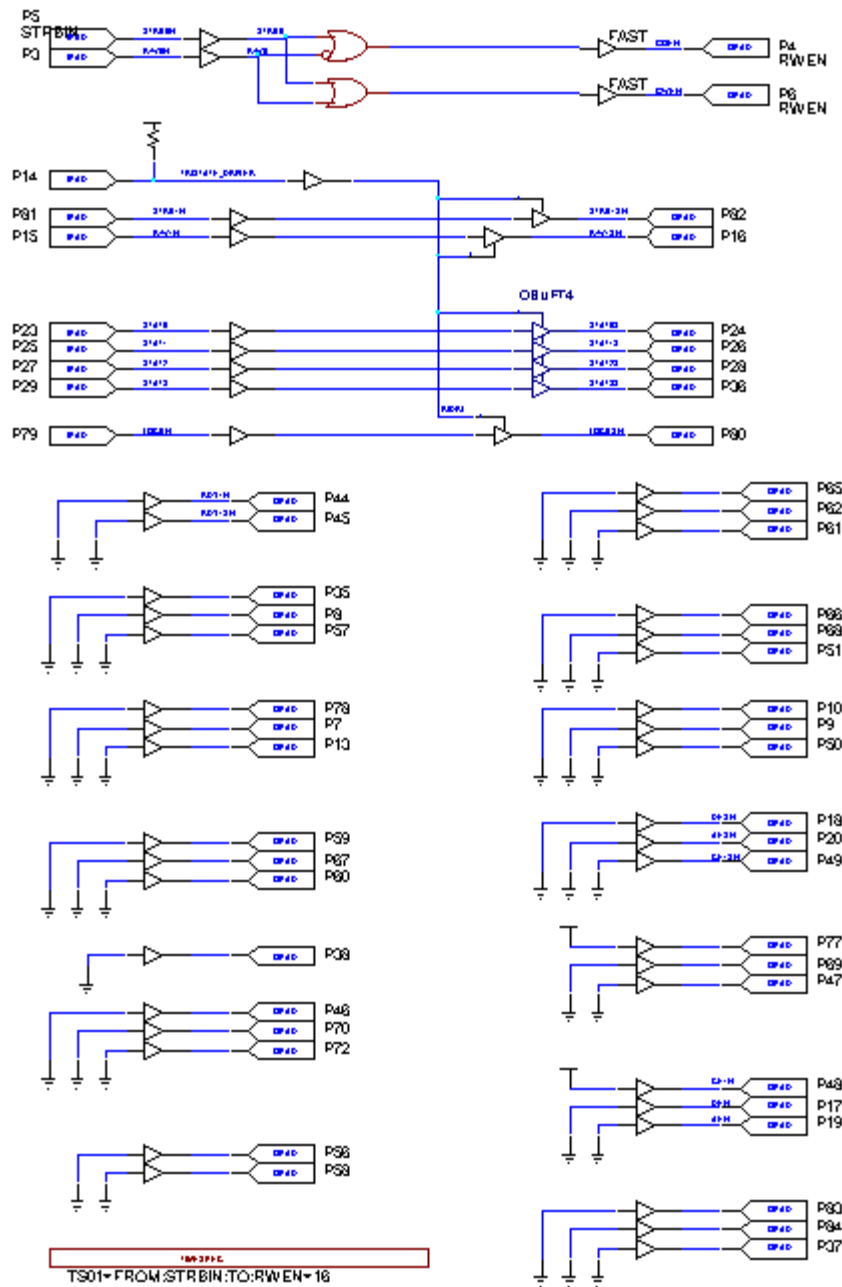


**Figure 4.6**

Top level schematic of the programmed logic for the Xilinx FPGA XC4003A-4PC84 to generate, buffer, and interface the control signals of the 'C40 global buses, and the non-volatile SRAM memory devices.

## Chapter 5

### Firmware and Software Development

In this chapter we discuss about all the firmware and software developed for the real-time wavelength modulated optical fiber sensor system. First we discuss about the development of the digital signal processing (DSP) routines, and then we discuss about the development of the Internet connectivity software.

#### 5.1 DSP Firmware and Software Development Environment

The Code Composer DSP Development System (version 5.0) for Windows, from GO DSP Corporation [Code95], and the Texas Instruments 'C4x DSP tools (the compiler, the assembler, the linker, the loader, and the ANSI C library functions) of version 4.70 are used for developing the DSP routines of our wavelength modulated optical fiber sensor system. Also used are some of the 'C4x SigTar [SigT93] and VecTar [Vect93] library functions of TARTAN Inc., presently a subsidiary of Texas Instruments Inc. The Mountain-510/LT Universal Emulator from White Mountain DSP Inc. is used for the hardware interface of our 'C4x system to the PC. The Mountain-510/LT uses the 'C4x JTAG connections, and is able to access (upload/download) any memory locations of the 'C4x system. The Code Composer must be configured with the software driver of the Mountain-510/LT to get access to the 'C4x system.

The Code Composer is a graphical user interface software, and is very handy to write, edit, compile, assemble, link, and load the program files of any project into the 'C4x system. It is also handy to see the contents of a certain memory range of the 'C4x system in a graph or window, to

see the values of all the CPU registers in a window, to halt the program flow at any certain location, to step through any program and display the code in the disassembly window, to monitor the values of variables from the watch window, and to animate any graph of memory values while the program is running. It also has features to halt the run time program execution at any particular memory or code location which make the program debugging very simple.

The Texas Instruments DSP tools allow mixed programming of C and/or assembly. We tried to develop our programs in C, except where extensive interfacing to registers is required or where using assembly saves considerable amount of execution time.

## **5.2 Development of the DSP Firmware and Software**

Appendix A lists all the DSP firmware and software routines developed for the stand alone real-time wavelength modulated optical fiber sensor system. Appendix A.1 and A.2 lists the signal processing routines for the EFPI sensor and the FBG sensor, respectively. Each sensor system has its own *main()* function, which calls all the DSP routines necessary for that particular sensor system. Some of the routines, e. g., the initialization routines and the data acquisition routine, are called by all the *main()* functions.

Presented below are the brief descriptions of all the signal processing routines called by the *main()* function of any wavelength modulated optical fiber sensor system.

### 5.2.1. The Initialization Routines

The initialization routines are called only once from the *main()* function. They are not executed as part of the real-time signal processing routines, rather they initialize the system memories only once at the system power on.

The function *vInitC4x()* initializes all the necessary CPU and peripheral bus registers of the 'C40 processor. The global memory interface control register (GMICR) and the local memory interface control register (LMICR) set the wait-states and the page sizes of the memory sections for the global and the local memory strobes, respectively. We require fully software controlled wait-count of 3 to access the STRB0 UART memory, wait-count of 0 to access the STRB1 SRAM, a wait-count of 1 to access the LSTRB0 non-volatile SRAM, and a wait-count of 7 to access the LSTRB1 watchdog timekeeper's memory. The interrupt flag register (IIF) is initialized to set the pin IIOF2 as a general purpose output signal, which is used as an enable input to the CCD spectrometer, to start and stop the trigger pulses required for the analog-to-digital conversions of the CCD video analog pulses. The Timer 0 control register and the Timer 0 period register are set to produce a 1.667 MHz of output clock signal at the TCLK0 pin. After setting the TCLK0 pin as an output clock, *vInitC4x()* waits for a while for the clock signal to be stable, before acquiring any data from the CCD spectrometer, as the TCLK0 signal is used as the input clock to the CCD spectrometer.

The function *vInitUART()* initializes all the necessary registers of the UART. It clears all the flags and removes all the characters, if any, by reading all the registers of the UART. *vInitUART()* then sets the baud rate for the UART by initializing the baud register.

The function *vCalbPxls()* initializes the array of 1024 floating point values with the corresponding calculated wavelengths of the 1024 elements (starting at element 17) of the Ocean Optics' CCD spectrometer. The first 14 CCD pixels, of the 1100-element spectrometer, are analog baseline and the next 2 pixels are ineffective photodiodes, and thus the first 16 pixel

elements are not active photodiodes. The coefficients for converting the pixel positions of the array into wavelengths are unique for any particular CCD spectrometer. The coefficients are provided by the Ocean Optics Inc., along with the CCD spectrometer.

### 5.2.2. The Data Acquisition Routine

The function *nAcqData(int \*iaData, int \*iaDMA3\_DEST, int \*iaDMA4\_DEST)*, acquires a set of 1100 integer data from the CCD spectrometer, using DMA interrupts, and saves them in an array pointed by *iaData*. As *nAcqData()* is implemented in assembly language, there are lots of ‘C40 register accesses involved in it, it is important to remember the order of argument transfers into the stack if we want to retrieve them from the assembly environment. In Texas Instruments’ ‘C40 compiler the rightmost argument is PUSHed first into the stack and the leftmost argument is PUSHed last. As the ‘C40 stack is of pre-incrementing, the leftmost argument has a higher address location in the stack than the rightmost argument.

As shown in Figure 4.1, each 12-bit digital datum is received in parallel by the ‘C40 communication ports 3 and 4. Communication port 4 receives the MS 8-bit of the datum, and the communication port 3 receives the LS 4-bit of the datum as the MS nibble, the LS nibble being permanently grounded. Even though the ‘C40 communication ports receive data in bytes, they are saved as 32-bit words, the first byte received being considered as the LS byte of the word. Thus the 1100 data set received by the communication ports 3 and 4, are first saved as two sets of 275 words, each word of any of these two sets having 4 bytes, each byte coming from a different datum. Note that at reset the ‘C40 communication ports 3, 4, and 5 are configured as input ports, and ports 0, 1, and 2 are configured as output ports.

The function *nAcqData()* first resets the DMA3 and DMA4 input queues, and then initializes all the DMA3 and DMA4 registers to receive 275 words each, at locations pointed by *iaDMA3\_DEST* and *iaDMA4\_DEST*, from the communication ports 3 and 4 respectively. DMA

is set to have a higher priority than the CPU. *nAcqData()* then enables the DMA interrupt and also enables the CCD spectrometer using the IIOF2 signal and waits in a loop and checks the DMA transfers until the 1100 data set is completely acquired or it may time out by counting down a predetermined number. It then disables both the CCD enable and the DMA interrupt enable, and calls the UNMINGLE subroutine, after proper register initializations, to unmingle the byte mingled data from two separate 275-word locations into a 1100 sign-extended 16-bit integer values, and to save that at location pointed by *iaData*. If *nAcqData()* times out in the wait loop, it returns with an error code of -1, otherwise if the data acquisition is successful it returns with a value of 0.

### 5.2.3. The UART Service Routine

The function *nServUART()*, if called, checks if there is any request for sending the set of acquired 1100 integer CCD data through the UART. If it finds the request 'S', it sends the 1100 data with the preamble (123456789) and the post-signature (987654321) and returns with a value of 0. Otherwise it returns with a value of -1.

The UART sends (or receives) data as characters. A 32-bit word integer is sent as 4 characters of 1 byte each. The routine is implemented such that the MS byte of the integer is sent first, and the LS byte of the integer is sent last. All the transfers are done through a hardware handshake, and can cause considerable delay in real-time implementations.

### 5.2.4. The EFPI Signal Processing Routines

The function *vFiltrBw3()* performs a high-pass filtering to the data with third order Butterworth coefficients having a normalized cutoff frequency of 0.02. The filtering primarily gets rid off the DC values present in the data.

The function *fftr()* is a Tartan SigTar optimized signal processing library function [Sig93]. It performs a 1024 point in-place fast Fourier transform (FFT) on the filtered data.

The function *cvabs()* is a Tartan VecTar vector math library function [Vect93]. It basically finds the magnitude of the complex FFT data returned by *fftr()*.

The function *maxv()* is also a Tartan VecTar vector math library function. It finds the maximum value of the magnitude of the complex FFT data, along with its index in the array.

The function *vFindFloatPix()* finds the index of the maximum value of the FFT magnitudes of the data more precise than just an integer. It makes a Gaussian approximation with three FFT magnitude values, the maximum value and the two values just either side of the maximum value, and tries to find the floating point index of the real peak, as if the points were continuous.

The function *vFindTruGap()* finds the gap of the EFPI sensor using the discrete lambda transform (DLT). It uses the ‘golden search rule’ [Press88], and the estimated gap to reduce the number of DLT transformation, as it is very computationally intensive if compared to other functions.

The function *vDGT()* performs the discrete gap transformation (DGT) on the data for the given EFPI gap, and finds the DGT magnitude for it.

### **5.2.5. The FBG Signal Processing Routines**

Appendix A.2 include the FBG signal processing routine, *vFindPks()*, used for the real-time FBG optical fiber sensor system. The function *vFindPks()* calculates the wavelength locations of all the Bragg peaks from the 1100 floating point data values using a centroid method, as discussed in

section 3.5. The number, the ranges, and the widths of the Bragg peaks must be provided with the function call.

### **5.2.6. The Memory Allocation File**

Appendix A.4 lists the memory allocation file (also known as *.CMD* file) required for the Texas Instruments' DSP tools to load programs on the 'C40 system. It first declares and assigns a name to all the valid addressable memory ranges, and then instructs the loader where to load different program sections in those memory ranges.

## **5.3 The TCP/IP Client/Server Software Development Environment**

All the TCP/IP client/server graphical user interface software were developed with the LabWindows-CVI (version 4.0) software environment of National Instruments Inc. It has extensive library support in the areas of user interfaces, RS232 communications, and the TCP/IP client/server communications. We used these library functions in C to implement the client/server software and hence to interface the real-time wavelength modulated optical fiber sensor system to the Internet

## **5.4 Development of the TCP/IP Client/Server Software**

Appendix B lists all the TCP/IP client/server software developed to interface our real-time wavelength modulated optical fiber sensor system to the Internet, as depicted in Figure 5.1. One is able to acquire the data through the Internet from the 'C40 system from anywhere in the world, by using this client/server software.

Given below are brief descriptions of the client/server routines developed to acquire data through the Internet from the 'C40 system in real-time.

#### **5.4.1 TCP/IP Client Programs**

Appendix B.1 shows the graphical user interface panel for the TCP/IP server, and B.2 lists the programs to run the client. When the client program is executed it prompts the user either for the name or the Internet Protocol (IP) address of the machine running the server. The program then prompts the user for the TCP/IP port number set for the server. It then loads the graphical user interface panel along with its menu and controls, and initiates a connection to the server. If the connection initiation is failed it lets user know about that and ends the graphical user interface and the program. If the connection initiation is successful it makes the color of a control button green to indicate that it is connected to the server. Using the pull-down menu of the client graphical user interface panel, one can send a request to the server to send the real-time 1100 integer data set of the CCD spectrometer from the 'C40 system. Upon receiving the data from the server, the client program displays it on the graph panel. One can also initiate a continuous request, in which case the graph panel is updated continuously with the real-time data.

The pull-down menu of the client panel also supports that any data set be saved in a file, or that any data set be read from a file and be displayed on the graph.

#### **5.4.2 TCP/IP Server Programs**

Appendix B.3 shows the graphical user interface panel for the TCP/IP server, and B.4 lists the programs to run the server. When the server is started it prompts the user to input the serial (RS232) communication port number to communicate to the 'C40 sensor system, and initializes

that port with the baud rate and other protocols supported by the UART of the 'C40 system. The program then prompts the user to input a TCP/IP port number for the server. This port number must be used by any client to make any connection to the server. The graphical user interface panel is loaded then, with its menu and controls, and runs the TCP/IP server, and waits for any TCP/IP client to make connection to it and to request data. If requested, it downloads the set of 1100 integer CCD data by checking the preamble and the post-signature of the data set, from the 'C40 system through the RS232 comport and transmits them to the client through the Internet. While downloading the 32-bit integer data as 8-bit characters, it must be remembered that the UART of the 'C40 system sends the MS-byte of each datum first and the LS-byte last. If any client is currently connected to the server, the server panel indicates that with a control button by changing its color to green.

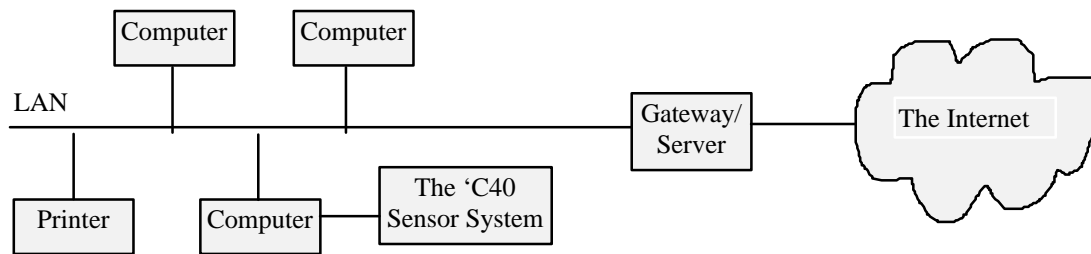


**Figure 5.1**

Block level diagram of the networking connections of the real-time wavelength modulated sensor system with the Internet.